Lawrence Berkeley National Laboratory

Title
Iron site occupancies in magnetite-ulvospinel solid solution: A new approach using XMCD

Permalink
https://escholarship.org/uc/item/6694759b

Author
Pearce, C. I.

Publication Date
2010-05-31

Peer reviewed

Iron site occupancies in magnetite-ulvöspinel solid solution: A new approach using XMCD

Carolyn I. Pearce[1], C. Michael B. Henderson[1,2], Neil D. Telling[1], Richard A.D. Pattrick[1], David J. Vaughan[1], John M. Charnock[1], Elke Arenholz[3], Floriana Tuna[4], Victoria S. Coker[1]and Gerrit van der Laan[1,5]

[1] *School of Earth, Atmospheric and Environmental Sciences and Williamson Research Centre for Molecular Environmental Science, University of Manchester, Manchester M13 9PL, UK*

[2] *Daresbury Laboratory, Warrington WA4 4AD, UK*

[3] *Advanced Light Source, Lawrence Berkeley National Laboratory, Berkeley, California 94720, USA*

[4] *School of Chemistry, University of Manchester, Manchester, M13 9PL, UK*

[5] *Diamond Light Source, Chilton, Didcot OX11 0DE, UK*

ABSTRACT

Ordering of Fe^{3+} and Fe^{2+} between octahedral (Oh) and tetrahedral (Td) sites in synthetic members of the magnetite (Fe_3O_4) – ulvöspinel (Fe_2TiO_4) solid-solution series was determined using Fe $L_{2,3}$-edge X-ray magnetic circular dichroism (XMCD) coupled with electron microprobe and chemical analysis, Ti L-edge spectroscopy, Fe K-edge EXAFS and XANES, Fe^{57} Mössbauer spectroscopy, and unit cell parameters. Microprobe analysis, cell edges and chemical FeO determinations showed that the bulk compositions of the samples were stoichiometric magnetite-ulvöspinel solid-solutions. Surface sensitive XMCD showed that the surfaces of these oxide minerals were more sensitive to redox conditions and some samples required re-equilibration with suitable solid-solid buffers. Detailed site-occupancy analysis of these samples gave XMCD-Fe^{2+}/Fe^{3+} ratios very close to stoichiometric values.

$L_{2,3}$-edge spectroscopy showed that Ti^{4+} was restricted to Oh sites. XMCD results showed that significant Fe^{2+} only entered Td when the Ti content was > 0.40 apfu while Fe^{2+} in Oh increased from 1 a.p.f.u in magnetite to a maximum of ~1.4 apfu in USP45. As the Ti content increased from this point, the steady increase in Fe^{2+} in Td sites was clearly observable in the XMCD spectra, concurrent with a slow decrease in Fe^{2+} in Oh sites. Calculated magnetic moments showed a steady decrease from magnetite (4.06 μ_B) to USP45 (1.5 μ_B) and then a slower decrease towards the value for ulvöspinel (0 μ_B). Two of the synthesized samples were also partially maghemitized by re-equilibrating with an oxidizing Ni-NiO buffer and XMCD showed that Fe^{2+} oxidation only occurred at Oh sites, with concomitant vacancy formation restricted to this site.

This study shows the advantage of using XMCD as a direct measurement of Fe oxidation state in these complex magnetic spinels. These results can be used to

rationalize the magnetic properties of titanomagnetites, and their oxidized titanomaghemitized analogues, in Earth's crustal rocks.

INTRODUCTION

The most important magnetic rock-forming minerals are oxides of iron and titanium and their compositions can be represented in the FeO-TiO_2-Fe_2O_3 ternary diagram in Figure 1 (Lindsley, 1976). Three major solid-solution series have been identified in this system: magnetite (Fe_3O_4) – ulvöspinel (Fe_2TiO_4) (the titanomagnetite series), hematite (α-Fe_2O_3) – ilmenite ($FeTiO_3$) (the titanohematite series) and pseudobrookite (Fe_2TiO_5) – ferropseudobrookite ($FeTi_2O_5$). The first series plays a major role in controlling rock magnetism and the palaeomagnetic properties of the Earth's crust (Banerjee, 1991; O'Reilly, 1984). The principal magnetic minerals crystallizing from basaltic magmas forming new oceanic crust are titanomagnetites, of ideal formula $Fe_{3-x}Ti_xO_4$, where $x \approx 0.6$ (O'Reilly, 1984) (Fig. 1). During subsolidus cooling of titanomagnetites under dry conditions, exsolution of titanohematite lamellae leaves a host phase richer in the magnetite component. At temperatures below ~600°C primary titanomagnetites interact with aqueous fluids and undergo oxidation and maghemetization, ultimately leading to the formation of ilmeno-hematites as the most stable magnetic phases at low temperatures and pressures. Under analogous conditions end-member magnetite initially oxidizes to form cubic maghemite (γ-Fe_2O_3) with hematite as the potential final product.

The technological importance of magnetic spinel structures and their geophysical significance has led to extensive investigations into their complex chemistry, structure, site occupancies, and relationships between atomic structure and physical properties. Particular attention has been paid to the influence of maghematization on the magnetic properties of titanomagnetites in oceanic basalts during hydrothermal alteration near spreading ridges (Bleil and Petersen, 1983; Zhou et al., 2001). The determination of multivalent transition element (most importantly Fe^{2+} and Fe^{3+}) distribution between tetrahedral and octahedral sites in spinel-group minerals is a huge challenge which has been addressed using many different techniques including chemical and electron probe microanalysis, X-ray and neutron single-crystal and powder diffraction (Bosi et al., 2009; Fujino, 1974; Wechsler et al., 1984), Mössbauer spectroscopy (Hamdeh et al., 1999), transmission electron microscopy (Zhou et al., 1999) and X-ray absorption spectroscopy (Henderson et al., 2007). In this study, the synchrotron-based technique of x-ray magnetic circular dichroism (XMCD) is used for the first time to investigate the complex problem of crystal structure in a series of fully characterized titanomagnetites.

THE STRUCTURE AND MAGNETIC PROPERTIES OF TITANOMAGNETITES

Titanomagnetites have a spinel structure (space group *Fd3m*), with 32 oxygens per unit cell arranged in cubic close-packed layers forming (111) planes of a face-centred cubic lattice defining two distinct cation sites with four or six nearest O neighbors. The general formula can be written as $A_8B_{16}O_{32}$, where A is in tetrahedral coordination and B is in an octahedral site. The cations (Fe^{2+}, Fe^{3+} and Ti) occupy 1/8

of all tetrahedral sites and 1/2 of all octahedral sites (O'Reilly, 1984). The distribution of cations between tetrahedral and octahedral sites minimizes the total lattice energy, with the lowest electrostatic energy being achieved when low valency cations occupy tetrahedral sites, forming a normal spinel. However, in end-member magnetite (Fe_3O_4), Fe^{3+} has a much stronger preference for the smaller tetrahedral site, which can be explained by its tendency to form hybrid sp^3 bonds (Goodenough and Loeb, 1955), relegating the Fe^{2+} ion and the other Fe^{3+} ions to the octahedral sites; magnetite is thus an $M^{3+}{}_A(M^{2+},M^{3+})_BO_4$, 'inverse' spinel. Titanomagnetites are solid-solutions series of magnetite and ulvöspinel in which Fe^{3+} in the B sub-lattice of magnetite are replaced by Ti^{4+}, with the concurrent conversion of Fe^{3+} to Fe^{2+} to maintain charge balance.

Magnetite is ferrimagnetic at room temperature with a Curie temperature of 850 K. The two different cation sites in the structure form two magnetic sublattices and the spin arrangement can be written as $(Fe^{3+}\downarrow)_A(Fe^{3+}\uparrow\ Fe^{2+}\uparrow)_BO_4$ (see e.g. Cornell and Schwertmann, 2003). As the magnetic contributions of the antiparallel Fe^{3+} spins on the A and B sites are cancelled out, the net ferrimagnetism results from the Fe^{2+} in the B sub-lattice. The net magnetization of magnetite is calculated from the difference in magnetic moment between the octahedral and tetrahedral sub-lattices, with one Fe^{3+} (5 μ_B) and one Fe^{2+} (4 μ_B) per formula unit on the octahedral sites, and one Fe^{3+} (5 μ_B) on tetrahedral sites to give $M_s = (5 + 4) - 5 = 4\ \mu_B$. Fully oxidized magnetite (γ-Fe_2O_3, maghemite) has an effective spinel formula of $Fe^{3+}{}_{2.666}\square_{0.333}O_4$ (where $\square$ represents vacancies) and gives an increased magnetic moment of 4.33 μ_B, resulting from the ordering of the vacancies into octahedral sites (Gillot, 1994).

In titanomagnetites, Fe^{3+} is replaced by Fe^{2+} in the A sub-lattice and Ti^{4+} in the B sub-lattice, reducing the net ferrimagnetism. This can be observed by the continuously decreasing Curie temperature through the solid-solution series (Akimoto, 1962). In end-member ulvöspinel, with a formula of $(Fe^{2+}\downarrow)_A(Fe^{2+}\uparrow)_BTiO_4$, the magnetic structure is perfectly antiferromagnetic so that the expected net magnetization is zero. Determining the net magnetization of oxidized titanomagnetites (titanomaghemites) is more complex as the magnetic moment depends on the site ordering of vacancies, as well as the site ordering of Fe^{2+}, Fe^{3+} and Ti.
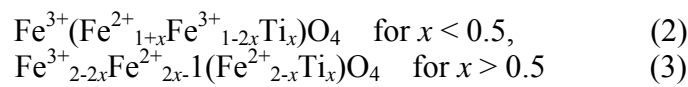
SITE OCCUPANCY MODELS OF TITANOMAGNETITES

Reliable knowledge of cation distribution in titanomagnetites is essential to understand the complex magnetic behaviour of these minerals, which includes magnetocrystalline anisotropy and spin canting (Hamdeh et al., 1999). Significant site disorder exists in spinels, thus the cation distribution in titanomagnetite solid solutions ($Fe_{(3-x)}Ti_xO_4$), (where x defines the proportion of ulvöspinel in the solid solution) is variable and has been the subject of a number of studies (Table 1). For each model, the variation in site occupancies for Fe^{3+} and Fe^{2+} in tetrahedral (denoted Td) and octahedral (denoted Oh) sites is given as an equation in which cations inside the parentheses occupy Oh sites and those outside the parentheses occupy Td sites. Fe^{3+} and Fe^{2+} site occupancies are also shown graphically as a function of titanium concentration (Ti atoms per formula unit) in Figure 2. Note that end-member magnetite does not contain any Fe^{2+} in tetrahedral sites in any of the work summarised here.
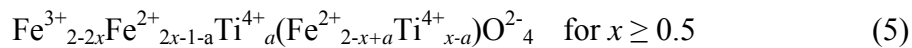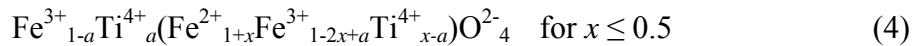
The Akimoto (1954) model (Table 1, Model A) proposed that the concentrations of Fe^{2+} and Fe^{3+} on both sites vary linearly with Ti content, x, according to the following equation:

$$Fe^{3+}_{1-x}Fe^{2+}_{x}(Fe^{2+}Fe^{3+}_{1-x}Ti^{4+}_{x})O^{2-}_{4} \qquad (1)$$
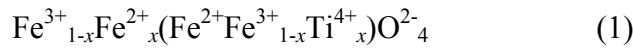
In this model Fe^{2+} Oh is fixed at 1 atom per 4 O. In direct contrast, Néel (1955) and Chevallier (1955) proposed a theoretical model (Table 1, Model B) based on Verwey's empirical law (Verwey and Heilman, 1947) concerning the preference of Fe^{3+} for tetrahedral sites in the spinel structure. The model assumed that Ti^{4+} always occupies octahedral sites and that the remaining octahedral sites are filled by Fe^{2+} ions. This was supported by a decrease in the saturation moment and the Curie temperatures with increasing Ti content (Néel, 1955). Thus, two substitution intervals can be defined as

$$Fe^{3+}(Fe^{2+}_{1+x}Fe^{3+}_{1-2x}Ti_{x})O_{4} \quad \text{for } x < 0.5, \qquad (2)$$
$$Fe^{3+}_{2-2x}Fe^{2+}_{2x-1}(Fe^{2+}_{2-x}Ti_{x})O_{4} \quad \text{for } x > 0.5 \qquad (3)$$

However, it was stated that the experimental data available were insufficient to confirm this theoretical model, especially with regard to the distribution of Fe^{2+} ions. In determining the magnetic properties of titanomagnetites in the $TiFe_2O_4 - Fe_3O_4$ solid-solution series from samples synthesized under known physico-chemical conditions, Akimoto et al. (1957) (Table 1, Model C) found that the saturation moments were intermediate between the values for the natural samples (Table 1, Model A) and the Néel-Chevallier theoretical values (Table 1, Model B). They concluded that this was due to some Ti ions entering into the tetrahedral sites (proportion denote by a) and that the cation distribution should then be considered as

$$Fe^{3+}_{1-a}Ti^{4+}_{a}(Fe^{2+}_{1+x}Fe^{3+}_{1-2x+a}Ti^{4+}_{x-a})O^{2-}_{4} \quad \text{for } x \leq 0.5 \qquad (4)$$

$$Fe^{3+}_{2-2x}Fe^{2+}_{2x-1-a}Ti^{4+}_{a}(Fe^{2+}_{2-x+a}Ti^{4+}_{x-a})O^{2-}_{4} \quad \text{for } x \geq 0.5 \qquad (5)$$

O'Reilly and Banerjee (1965) (Table 1, Model D) concluded that the cation distribution is governed by the preference of Fe^{3+} for tetrahedral sites in the range $0 < x < 0.2$ (cf. equation (2) above). However, this preference is partially outweighed by the increase in electrostatic energy obtained by placing Fe^{2+} in tetrahedral sites in the range $0.2 < x < 0.8$, giving the following configuration of cations

$$Fe^{2+}_{x-0.2}Fe^{3+}_{1.2-x}(Fe^{2+}_{1.2}Fe^{3+}_{0.8-x}Ti^{4+}_{x})O^{2-}_{4} \qquad (6)$$
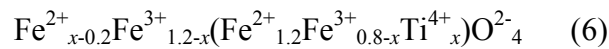
while all of the Fe^{3+} is located in tetrahedral sites for $0.8 < x < 1$ cf. equation (3).

Values of the saturation magnetization and individual sublattice magnetic moments obtained by Weschsler et al. (1984) (Table 1, Model E) suggest that the average Fe^{2+}-Fe^{3+} site occupancies vary linearly with composition, and are consistent with the cation distribution model of Akimoto (1954) (Table 1, Model A), which requires that Fe^{2+} is present in exactly 1/2 of the occupied Oh sites for all compositions and that $Fe^{3+}(A)$ exactly equals $Fe^{3+}(B)$, but with a possible slight Oh preference for Fe^{2+} (equal to the slight Td preference for Fe^{3+}) in the low-Ti region. The values do not support models that propose a quenchable, temperature-dependent Fe^{2+}-Fe^{3+}

distribution. Variations from the Akimoto model are attributed to incomplete homogenization of the materials during synthesis.

Kąkol et al. (1991) (Table 1, Model F) proposed a Fe^{3+}-Fe^{2+} cation distribution determined indirectly from saturation-magnetization data, assuming values of $4.06\mu_B$ and $5\mu_B$ for Fe^{2+} and Fe^{3+}, respectively. It is postulated that, up to the composition limit $x = 0.2$, the tetrahedral sites are occupied exclusively by Fe^{3+} ions; the conversion of Fe^{3+} into Fe^{2+} ions arising from Ti^{4+} substitution occurs solely on octahedral sites, in agreement with the Néel-Chevallier and O'Reilly-Banerjee models. At higher Ti^{4+} concentration, Fe^{3+} and Fe^{2+} ions occupy both sites and their relative concentrations vary linearly with x. Thus, the cation distribution is given by

$$Fe^{3+}(Fe^{3+}_{1-2x}Fe^{2+}_{1+x}Ti^{4+}_x)O^{2-}_4 \quad \text{for } 0 \leq x \leq 0.2 \qquad (7)$$

$$Fe^{3+}_{1.25-1.25x}Fe^{2+}_{1.25x-0.25}(Fe^{3+}_{0.75-0.75x}Fe^{2+}_{1.25-0.25x}Ti^{4+}_x)O^{2-}_4 \quad \text{for } 0.2 < x \leq 1 \quad (8)$$

Hamdeh et al. (1999) (Table 1, Model G) used peak area analyses of Mössbauer spectra to define three different Fe^{2+} and Fe^{3+} distribution regions in the equation

$$Fe^{3+}_{f(3-x)}Fe^{2+}_{1-f(3-x)}(Fe^{3+}_{2(1-x)-f(3-x)}Fe^{2+}_{x+f(3-x)}Ti_x)O_4 \qquad (9)$$

with $f = 0.333(1-0.25x)$ for $0 < x < 0.2$, $f = 0.35(1-0.57x)$ for $(0.3 < x < 0.5)$, and $f = 0.50(1-x)$ for $(0.5 < x < 1)$.

Hamdeh et al. (1999) also calculated the saturation moments, assuming $4.06 \mu_B$ for Fe^{2+} and $5 \mu_B$ for Fe^{3+}, for comparison with other models and obtained good agreement with magnetization measurements conducted by Kąkol et al. (1991) for $x \leq 0.5$. However, their results deviated for lower values of x due to the presence of α-Fe_2O_3, detected by XRD, which also has implications for their distribution model.

Bosi et al. (2009) (Table 1, Model H) suggested that the cation distribution can be split into two contributions: a linear trend due to the Fe^{3+} T_d + Fe^{3+} O_h = Fe^{2+} T_d + Ti^{4+} O_h chemical substitution (cf. Akimoto 1954) and a non-linear trend due to internal electron exchange. It is suggested that the S-shaped trend centred at ~70%USP is due to reversal in the direction of electron exchange from Td to Oh for magnetite-rich samples to Oh to Td for ulvöspinel-rich samples.

These eight models reveal the many complexities surrounding the relationship between cation distribution and magnetic properties in titanomagnetites. They contain, however, a number of concerns relating to sample preparation and data manipulation, whilst the cation-site occupancies were either indirectly obtained from magnetic measurements or by interpretation of non-unique diffraction or spectroscopic measurements. In this study, the element-specific technique of X-ray magnetic circular dichroism (XMCD) has been used to provide more direct information about the oxidation state (including mixed states), site symmetry, spin state, and crystal-field splitting of the absorbing $3d$ transition metal ions.

A NEW APPROACH USING X-RAY MAGNETIC CIRCULAR DICHROISM AT THE Fe $L_{2,3}$ EDGE

XMCD has been used extensively to study the links between magnetic properties and cation site occupancies in iron oxide thin films and multilayers, including stoichiometric magnetite and vacancy-rich maghemite (Pellegrin et al., 1999; Schedin et al., 2000). More recently, XMCD has provided important new information on natural magnetic spinels and synthetic analogues (Pattrick et al., 2002; Pearce et al., 2006), as well as biogenic magnetite (Coker et al., 2008) and cobalt ferrite (Coker et al., 2009). XMCD is the difference spectrum of two X-ray absorption spectra (XAS) taken in a magnetic field, and is obtained by changing the direction of the circularly polarized light or reversing the direction of the applied magnetic field. XMCD offers unique advantages over other existing techniques since the atomic transitions in X-ray absorption occur on a timescale shorter than the electron hopping, making it possible to distinguish the different oxidation states of the tetrahedral and octahedral Fe ions (Pattrick et al., 2002). The Fe $L_{2,3}$-edge is probed using soft X-rays (~707eV) in total-electron yield (TEY) detection mode providing information on an effective probing depth of ~4.5 nm. The surface-sensitive nature of this technique, when combined with detailed characterization of the bulk material using XRD and EPMA, provides a powerful tool to fully describe the cation distribution in titanomagnetites. In this paper, the results of a detailed XMCD study of synthetic members of the ulvöspinel-magnetite solid solution series is presented and these results are supplemented with magnetic measurements, Mössbauer and XAS spectroscopic data for selected samples. A new site occupancy model, based on XMCD, is proposed and the effect of oxidation on selected synthetic samples is examined.

EXPERIMENTAL TECHNIQUES
Synthesis

Samples were prepared in 5 g batches by grinding together stoichiometric mixtures of powders of high purity TiO_2, Fe_2O_3, and iron metal under acetone for about 30 minutes. Each powder was divided into two portions and loaded into silver capsules which were crimped and sealed under vacuum in separate quartz glass tubes; a plug of pure silica wool was used to keep the silver tubes at the bottom of the silica tubes. Samples were heated at 900°C for at least 7 days before quenching in air. One sample tube of a pair was opened and XRD was used to assess the quality; the other tube was kept sealed and under vacuum until immediately before the XMCD data collection.

Two samples sets were synthesized in the solid solution series $Fe_{3-x}Ti_xO_4$. Set 1 was run for 11 days and consisted of samples with $x = 0.2, 0.4, 0.6$ and 0.8 (USP20/1 etc.); all were single-phase spinels. Set 2 ($x = 0.15, 0.30, 0.45, 0.60, 0.75, 0.90$, and 1.0; USP15/2, etc.) was heated for 8 days. The samples in set 2 were homogeneous, single-phase spinels with the exception of USP15/2, which contained a small impurity of a spinel with less Ti that the nominal bulk composition, and of USP100/2, which contained a small amount of ilmenite.

Whilst EPMA, XRD and chemical analysis for FeO of the bulk samples indicated that they were stoichiometric, XMCD analysis of the top ~4.5 nm showed that the sample surface was more reduced with respect to stoichiometry at the magnetite-rich end of the solid-solution series and more oxidized at the ulvöspinel-rich end. Thus, small amounts (~50 mg) of the samples were loaded into silver tubes, crimped and heated in evacuated silica tubes at 900°C for ~2 h in the presence of a range of solid-solid

buffers with different oxygen fugacites (in separate, crimped Ag tubes) to control the redox conditions and restore the surface stoichiometry. For samples with x between 0 and 0.6, either nickel-nickel oxide or quartz-fayalite-magnetite was used as an oxidising buffer and for samples with x between 0.6 and 1.0, wustite-magnetite-iron was used as a reducing buffer.

Electron probe microanalysis (EPMA) and chemical analysis

Portions of the samples used for XMCD were mounted analyzed using a Cameca SX100 electron microprobe. About 10-20 spot analyses were obtained for each sample using a 2 μm diameter electron beam with beam conditions of 15 keV and specimen current of 20 nA; standards used were fayalite and rutile. Full ZAF corrections were carried using the Cameca PAP routine. Mean wt % analyses (1 σ given in brackets) are given in Table 2. Bulk Fe is reported as FeO (Table 2) so that analytical totals increase progressively from the magnetite-rich to the ulvöspinel-rich samples reflecting the higher Fe_2O_3 contents of the former. Atomic cell formulae calculated to 32 oxygens invariably total more than 24 cations resulting from the deficiency of O which should have been allocated to Fe^{3+}. The cell formulae given in Table 2, given together with the molar ulvöspinel content (USP%), are recalculated to 32 oxygens and a total of 24 cations (Droop, 1987) which allows contents of Fe^{2+} and Fe^{3+} to be defined; note that this calculation fixes the reported compositions to be stoichiometric so that they lie exactly on the magnetite-ulvöspinel join in the system TiO_2-FeO-Fe_2O_3 (Fig. 1). Chemical analyses for FeO, obtained using the ammonium metavanadate method (Wilson, 1955), are given for most samples and stoichiometric FeO contents are also given showing good agreement, generally within analytical error. Overall, the chemical data show that the samples are homogeneous and close to the nominal compositions but the dominant composition inUSP15/2 is ~USP17 with the mismatch accounted for by a small amount of a less Ti-rich spinel. The presence of ilmenite in USP100/2 causes the spinel phase in this sample to be off-composition. Note that the two separate USP60 samples (USP60/1 and USP60//2) have identical stoichiometry.

X-ray powder diffraction (XRD)

X-ray powder diffraction was used to characterize the crystallization products and to determine unit cell parameters. Silicon was used a calibrant. The cell parameters (1 σ given in brackets) are given in Table 2 and the unit cell data of Akimoto (1957) are used to assign bulk compositions to the samples. The XRD derived compositions are very close to the EPMA values.

$L_{2,3}$-edge X-ray absorption spectroscopy (XAS) and X-ray magnetic circular dichroism (XMCD)

X-ray absorption spectra were collected on beamline 4.0.2 at the Advanced Light Source (ALS), Berkeley, CA, using the eightpole magnet endstation (Arenholz and Prestemon, 2005). The samples were maintained in the evacuated silica synthesis tubes until they were required for measurement. The powders were removed from the tubes in an anaerobic cabinet and ground to a powder, using a silica pestle and mortar. The powders were then mounted on carbon tape attached to the sample manipulator and loaded into the endstation under anaerobic conditions. The sample was positioned

with the X-ray beam entering parallel to the magnetic field and perpendicular to the sample surface. Samples $\geq$USP75 were measured at 180 K, all other measurements were made at room temperature.

The XAS signal was monitored in total-electron yield mode, giving an effective probing depth of ~4.5 nm. At each energy point the XAS was measured for the two opposite magnetization directions by reversing the applied field of 0.6 T. The XAS spectra of the two magnetization directions were normalised to the incident beam intensity and subtracted from each other in order to obtain the XMCD spectrum (Pattrick et al., 2002). The measured Fe $L_{2,3}$ XMCD was used to extract the site occupancies and oxidation state of the cations in the spinel structure of the titanomagnetite. At the transition metal $L_{2,3}$ edge, the $2p$ core electrons are excited by electric-dipole transitions into (partially) localized unoccupied $3d$ states, providing information about the local electronic and magnetic structure of the absorbing atom through measurement of the XMCD (van der Laan and Thole, 1991). The spectrum is split by the $2p$ spin-orbit interaction into two main structures, the L_3 and L_2 edge. For titanomagnetite, the Fe L edge XMCD has four main peaks in the L_3 edge XMCD with positive, negative, positive and negative signal which are related to the amounts of Fe d^6 Td (~709eV), d^6 Oh (710 eV), d^5 Td (~711eV) and d^5 Oh (~712eV), present in the sample.

To obtain the relative amounts of the four Fe sites, the experimental spectra were fitted by means of a nonlinear least-squares analysis, using calculated spectra for each of the Fe sites. In these calculations, as described in (van der Laan and Thole, 1991), the Hartree-Fock-Slater integrals for the $3d,3d$ and $2p,3d$ Coulomb and exchange interactions were scaled to 70% and 80%, respectively, and the magnetic exchange field was taken equal to $g\mu_BH = 0.05$ eV. The calculated atomic Hartree-Fock value of the $2p$ core-hole spin-orbit splitting was increased by 1.63% to fit the experimental value of 12.5 eV. For magnetite the crystal-field parameter $10Dq$ for the Oh and Td sites was taken as 1.2 eV and -0.6eV, respectively, and this parameter was slightly changed depending on the Ti content. The spectra were calculated at room temperature (RT corresponds to 26 meV) by summing over the initial-state energy levels using a Boltzmann distribution. While the shape of the calculated spectra of Fe d^6 Oh and Td depends on the temperature and magnetic exchange field, the spectra for Fe d^5, with its half-filled shell, are rather insensitive to these parameters. The calculated spectra were convoluted by a Lorentzian of $\Gamma = 0.3$ (0.5) eV for the L_3 (L_2) edge to account for intrinsic core-hole lifetime broadening together with a Gaussian of $\sigma = 0.15$ eV to account for instrumental broadening. The experimental spectra were fitted over the L_3 main peaks only, which has previously been shown to give meaningful results, although fitting over the L_2 peak does give good qualitative agreement (Pattrick et al., 2002; Pearce et al., 2006). The estimated random error per cation site occupancy value is $\pm$ 0.02 (Coker et al., 2009), however there is a systematic error associated with the incorporation of the fourth Fe d^6 Td site which is difficult to estimate.

The Ti $L_{2,3}$ XAS was also recorded on beamline 4.0.2. at the ALS and is not sensitive to the magnetic field.

K-edge X-ray absorption near edge spectroscopy (XANES) and extended X-ray absorption fine structure (EXAFS)

XAS data for the titanomagnetites were collected at the Fe *K*-edge on station 9.3 of the STFC Daresbury Synchrotron Radiation Source (SRS), operating in continuous scanning (QEXAFS) transmission mode. A double-crystal Si(111) monochromator was used, detuned to 50% transmission to minimize harmonic contamination. The samples were prepared by grinding, diluting with boron nitride to give an edge step of ~1, and mounting in 1mm thick Al sample holders with Sellotape windows; four 15 min scans were recorded and averaged for each sample. During data acquisition the samples were maintained at ~80K in a liquid nitrogen cooled cryostat. Energy calibration was provided by collecting data from a sample of end-member magnetite which had previously been measured with respect to an Fe foil (Henderson et al., 2007).

XANES data were prepared by fitting a first-order polynomial to the pre-edge region, extrapolating and subtracting this from the whole spectrum. Two third-order polynomials were fitted to the post edge region, joining smoothly at the node, subtracted from the spectrum, and the edge-step normalized to a value of 1. Background subtracted EXAFS spectra were analyzed in EXCURV98 using full-curved-wave theory (Binsted, 1998; Gurman et al., 1984). Phase shifts were derived in the programs from *ab-initio* calculations using Hedin-Lundqvist potentials and von Barth ground states (Hedin and Lundqvist, 1969). The structure of magnetite was used to set up a model comprising 13 shells around the central Fe absorber atom (Henderson et al., 2007) and the absorber-scatter distances, the Debye-Waller factors and an energy correction Ef were refined to minimise the residual R-factor (Binsted et al., 1992). For shell 3 ($M_{Oh} - M_{Oh}$ interaction) and shell 4 ($M_{Oh} - M_{Td}$) the scatterers were modeled as composite Fe/Ti scatterers, weighted and averaged assuming all the Ti was in octahedral coordination with a random distribution of Ti and Fe around the available octahedral sites. For example, for USP30 (bulk Fe:Ti ratio 90:10) the scatterer in shell 3 has an Fe:Ti ratio of 85:15 and the ratio for the scatterer in shell 4 is 92:08. Equivalent data for USP60 are Fe:Ti 70:30 and 82:18, and for USP90 are 55:45 and 71:29.

Superconducting Quantum Interference Device (SQUID) magnetometry

Magnetic measurements were performed on polycrystalline samples restrained in eicosane, using a Quantum Design MPMS-XL SQUID magnetometer equipped with a 7 T magnet (School of Chemistry, University of Manchester). Field-cooled (FC) magnetization curves were recorded over 5 – 300 K temperature range with an applied magnetic field of 100 Oe. The diamagnetism of the sample holder and of eicosane was measured and extracted from the raw magnetic data.

<center>RESULTS AND DISCUSSION</center>

Chemical analyses and unit cell data

Unit cell parameters are given in Table 2 and plotted in Figure 3; the cell–edge *vs* chemical composition trend for the synthetic samples is very similar to published data. The data of Akimoto (1957) were used to assign bulk compositions to the samples synthesized in this study and, as expected, the compositions derived from cell edges are very close to the EPMA analyses.

As mentioned earlier, XMCD data for some samples showed more oxidized compositions than expected. Because of the surface sensitivity of the XMCD technique, it is possible that this was caused by the presence of an oxidized surface layer on the sample grains. In order to assess the scale of the oxidation, the second series of synthesized samples were chemically analyzed (in duplicate) for FeO. The chemical FeO values are generally within error of the stoichiometric values (Table 1). Based on the sample characterization, it was concluded that the bulk solid-solution samples were stoichiometric, ranging from ulvöspinel contents of 17% to 94%.

XANES and EXAFS

The Fe *K*-edge XANES spectra of the three titanomagnetites and an end-member magnetite (MT6P) are plotted in Figure 4; details of the pre-edge feature (1s-3d) are shown in the inset. EXAFS spectra and Fourier transforms are displayed in Figure 5 while near-edge and EXAFS data are summarised in Table 3. Interpretation of data is based on standard values for Fe-O bondlengths [and pre-edge heights] for Fe^{2+} and Fe^{3+} in tetrahedral and octahedral coordination from Henderson et al. (1995, 2007):

Fe^{2+} (Td) 2.00 Å [0.05]; Fe^{2+} (Oh) 2.11 Å [0.02]
Fe^{3+} (Td) 1.88 Å [0.12]; Fe^{3+} (Oh) 2.01 Å [0.02]

It is clear that with increasing ulvöspinel content the edge shifts to lower energy as the average oxidation state of the Fe decreases (Figure 4 and Table 3). The height of the pre-edge feature also decreases and is lower in energy reflecting both the decrease in oxidation state and the decrease in tetrahedral Fe^{3+}. In the EXAFS and Fourier transform (Figure 5), the main differences between the spectra are manifest in the peaks in the Fourier transform at ~1.8-2.1 Å (due to shells 1 and 2, the Fe_{Td}-O and Fe_{Oh}-O inner coordination sphere), at ~3 Å (shell 3, the Fe_{Oh} − Fe/Ti_{Oh} interaction) and at ~3.5 Å (shell 4, the Fe_{Td} − Fe/Ti_{Oh} plus Fe_{Oh} − Fe_{Td} interaction). The fitting parameters for these four shells are given in Table 3. In end-member magnetite the Fe-O interactions include contributions from Fe(III) in the tetrahedral site and both Fe(II) and Fe(III) in the octahedral site. The EXAFS contribution from the inner shells was modelled with just two components, representing an average tetrahedral and an average octahedral site – the additional parameters necessary to model a three or four component Fe-O peak were not statistically justified by the data.

The pre-edge height for end-member magnetite (0.05) matches the mean of heights for 1 atom Fe^{3+} in Td [0.12], 1 atom Fe^{3+} in Oh [0.02] and 1 atom Fe^{2+} in Oh [0.02]; the measured tetrahedral Fe-O bondlength of 1.89 Å is that for Fe^{3+} (Td) and the octahedral Fe-O bondlength of 2.05 Å is within error of the mean of Fe^{3+} (Oh) and Fe^{2+} (Oh). For USP30 the edge step and tetrahedral Fe-O bondlength are not significantly different from those for magnetite suggesting that little of no Fe^{2+} is present in Td. However, for USP30 the longer Fe-O_{Oh} bond length is consistent with the bulk of Fe^{2+} being in Oh. For the other two titanomagnetites, the Fe-O bond lengths in both Td and Oh increase with increasing Ti + Fe^{2+} substitution, reflecting the decrease in the average oxidation state of iron in both sites. The tetrahedral Fe-O bondlength for USP60 is consistent with ~0.25 atoms Fe^{2+} in Td while that for USP90 implies ~0.85 atoms Fe^{2+} in Td. In the whole series the Debye-Waller factors for the Fe − O scattering increase for both sites, which may be due to an increase of static disorder resulting from the replacement of Fe^{3+} by Fe^{2+} and Ti.

The Fe-(FeTi)$_{oct}$ distance for shell 3 shows little significant change (Table 3) due to simultaneous entry of larger Fe^{2+} and smaller Ti^{4+} into Oh. The shell 4 distance seems to show a small increase with increasing ulvöspinel content, which is presumably controlled by the increase in size of the tetrahedral site as larger Fe^{2+} progressively replaces smaller Fe^{3+}. In order to fit the amplitudes for shells 3 and 4 in the titanomagnetite solid solutions, the Debye-Waller factor must decrease slightly in shell 3 but increase slightly in shell 4 with increasing titanium. The different trend directions for the two sites implies changes in the static disorder rather than thermal disorder around each site, with the octahedral-octahedral distances becoming more ordered, and the octahedral-tetrahedral distances more disordered with increasing titanium. These differences can be rationalised by drawing attention to the fact that shell 3 results from interactions between the target atom Fe in Oh (consisting of both Fe^{3+} and Fe^{2+}) and an outer shell of Fe^{2+}, Fe^{3+}, and Ti randomly substituted on the Oh site. Apparently, the increase of Ti (and Fe^{2+}) in the solid solution series produces a more symmetrical environment in Oh and hence the decreasing Debye-Waller factor. By contrast, shell 4 results from interaction between Fe^{2+} and Fe^{3+} in Td (note that no Ti occurs in this site; Wechsler et al. (1984), see later) and an octahedral shell of Fe^{2+}, Fe^{3+}, and Ti and between Fe^{2+} and Fe^{3+} in Oh and Fe^{2+} and Fe^{3+} in Td. Such complexities lead to less symmetrical scattering environments for shell 4, and thus increasing Debye-Waller factors from USP30 to USP90.

SQUID

The magnetization of the series from USP30 to USP90 in the range 5-300 K is shown relative to the value at 5K in Figure 6. The Curie temperatures, determined for the samples with the highest Ti concentrations, were 282 K for USP75 and 174 K for USP90. These values plot on the curve showing the relation between the Curie temperature and chemical composition in Akimoto's Fe$_3$O$_4$-Fe$_2$TiO$_4$ solid solution series (Akimoto, 1962) and are consistent with the magnetization measurements made by Kąkol et al. (1991).

XMCD and XAS

The SQUID data (Fig. 6) showed that the Curie temperature of the samples decreased continuously with increasing Ti content, reaching RT for samples above USP75, in agreement with published data (Akimoto, 1962). XMCD measurements also showed that, at RT, the signal became progressively weaker (lower signal to noise) with increasing Ti content. Thus, for the samples USP75 and USP90, the XMCD measurements were carried at low temperature (140K).

The element-specific Fe $L_{2,3}$-edge XMCD spectra provide information on how the bulk Fe component is distributed between Fe^{3+} and Fe^{2+} in each of the crystallographically distinct Td and Oh sites. Before absolute values are deduced it is necessary to establish the structural site occupied by Ti. X-ray and neutron diffraction structural studies (Fujino, 1974; Wechsler et al., 1984) and XAS (Pearce et al., 2006) indicate that Ti only occurs in octahedral sites; the neutron data are particularly persuasive because of the distinct scattering lengths of Ti (-0.34 fm) and Fe (+0.95 fm). Ti L-edge XAS measurements were also made for the synthetic samples in this study to confirm the Ti site occupancy. Figure 7 shows representative data and all samples have the distinctive four-peak spectrum typical of Ti^{4+} in octahedral

coordination; the relative peak intensities and shapes suggest that Ti occupies symmetrical octahedral sites throughout the solid solution series. The experimental spectra agree well with the calculation for octahedral site symmetry with 10Dq close to 2 eV (Pearce et al., 2006; van der Laan and Kirkman, 1992). A non-cubic crystal field symmetry would lead to an additional splitting of the peaks (van der Laan, 1990), which is not observed in the case of titanomagnetites.

XMCD spectra for samples across the solid-solution series are shown in Figure 8. The technique showed that, within the probing depth of ~4.5 nm, some samples did not have the ideal Fe^{2+}-Fe^{3+} ratio. By controlling oxygen fugacity using a series of oxidizing or reducing buffers, samples were produced with measured Fe^{2+}/totalFe ratios as close as possible to stoichiometric values at this probing depth (see Table 4). However, for some samples the as-synthesized material (USP30SYN, USP45SYN and USP75SYN) have similar XMCD spectra to those for buffered samples (USP30QFM, USP45QFM, USP75(MW(F)). The ternary diagram in Figure 9 shows that samples are on-composition with respect to the magnetite (Fe_3O_4) – ulvöspinel (Fe_2TiO_4) solid-solution. Clear changes through the solid-solution series can be seen in the XMCD spectra (Fig. 8) with complexity increasing as Ti contents increase, reflecting increased proportions of Fe^{2+} in tetrahedral sites.

The XMCD spectra for synthetic and natural stoichiometric 'end-member' magnetites are well understood and show excellent agreement with theoretical spectra (e.g., Sette et al., 1990; Kuiper et al., 1997; Pattrick et al., 2002; Pearce et al., 2006). The XMCD spectrum for USP0 was fitted with the typical three peak structure for the end-member magnetite as represented by the L_3 region of the absorption spectrum (705-715eV) in Figure 8. The distinct peaks at ~710 (-ve), 711 (+ve), and 712 (-ve) eV are assigned to Fe^{2+} Oh, Fe^{3+} Td and Fe^{3+} Oh, respectively, but the prepeak structure shown in the experimental spectrum below ~708eV is not adequately fitted by current theory. Samples up to and including USP30 were fitted with this three peak structure and the proportions of the three components used to fit the experimental spectrum for USP30 are shown in Figure 10(B). The titanomagnetites, however, must contain a tetrahedral Fe^{2+} component in the Ti-rich samples as the end-member ulvöspinel ($Fe^{2+}_2TiO_4$) has one atom Fe^{2+} in each of the tetrahedral and octahedral sites and one atom of Ti in octahedral sites. The excellent spectral resolution of beamline 4.0.2. at the ALS enable the resolution of the complex structure at the low energies in the Fe $L_{2,3}$-edge spectra where the peaks for Fe^{2+} in tetrahedral and octahedral sites are located. Figure 10(A) shows the best-fit spectrum for USP75 and the decomposition into the spectra for the Fe^{2+} T_d, Fe^{2+} O_h, Fe^{3+} T_d, and Fe^{3+} O_h components is given (Fig, 10(B)). The spectrum for USP60 (Fig. 8) shows a clear peak at ~709eV (+ve) which is due to Fe^{2+} Td and the Fe^{3+}Oh peak shows a shoulder on the high-energy side at ~710.5 eV. With increasing Ti content the peak at 709eV becomes larger and the shoulder develops into new -ve and +ve peaks near 710.5 eV. The complexity in the spectra near 710.5 eV reflects the inter-relationship between the Fe^{2+} Td and Oh spectra. Fitting a Fe^{2+} Td component to the experimental spectrum only becomes reliable for samples ≥USP45/3, with the clear small +ve peak at 709 eV (Fig. 8). However, in sample USP30 a small upturn can be identified at 709eV which correlates with the presence of a minor amount of Fe^{2+} Td in this sample; the amount of this component is estimated by adding enough Fe^{2+} Td to fit the top of this upturn and its high energy flank (see Fig. 8). Similar, but much smaller 'upturns' are visible in USP15 and USP20 (Fig. 8) and these might represent very small amounts of

$Fe^{2+}Td$ in these samples. Because of the inter-relationship between the peaks for the four Fe components, the errors vary for different components but the estimates for the amounts of $Fe^{2+}Oh$ are the most reliable and are likely to have errors not more than $\pm$ 0.02.

Some explanation is required regarding how the fitted XMCD peak areas are used to derive crystal-chemically constrained site occupancy data. The first step is to scale the four individual peak areas so that the total area is equivalent to the analyzed Fe content i.e. Fe apfu = 3 - Ti apfu (the experimental spectra and the fits are shown in Figure 8 and the occupancy values are given in Table 4). The Fe site occupancies are plotted versus Ti (apfu) in Figure 11. Note that the experimentally determined XMCD Fe^{3+} and Fe^{2+} octahedral occupancies for the synthetic USP0 sample are 0.97 and 1.08, respectively, rather than 1.0 and 1.0, giving a sense of the scale of the systematic error. Thus the $Fe^{2+}Oh$ value increases from 1.08 for USP0 to as high as 1.46 at ~USP40 before falling steadily towards the ulvöspinel composition. These data show that Fe^{2+} only enters Td sites in significant amounts when Ti > ~0.4 a.p.f.u.; thus Fe^{2+} initially enters octahedral sites and peaks at ~1.4 a.p.f.u. in the USP45 sample. As the Ti content increases further, Fe^{2+} in Td increases steadily to ~USP60, and then more rapidly from USP60 to USP90. Tetrahedral Fe^{3+} shows the inverse relationship to that for $Fe^{2+}Td$ while $Fe^{3+}Oh$ shows a rapid decrease from magnetite towards USP30 and then a slower decrease towards the ulvöspinel end- member. Fe^{2+} in Oh decreases, trending towards 1.0 atom in each site in end-member ulvöspinel.

In these experimentally-derived XMCD data, the sums of Fe allocated to Td range from ~0.9 in magnetite-rich samples to ~1.1 in ulvöspinel-rich samples and therefore the total occupancies of Oh (Fe+Ti) therefore range from ~2.1 in magnetite-rich to ~1.9 in ulvöspinel-rich samples. Thus, these data reveal deviations from the expected spinel stoichiometry. For the high Ti samples these deviations could be caused by preferential spin canting of octahedral site moments, as has been seen previously in iron oxide materials (Brice-Profeta et al., 2005; Signorini et al., 2006) and requires further investigation. To compare these data with previous models, it is necessary to constrain the occupancy of Td to equal 1.0 per 4 O and the occupancy of Oh to be 2.0 per 4 O in the spinel structure and the site occupancies determined from XMCD have been recalculated on this basis. These crystal-chemically constrained Fe site occupancies are the ones used in Figure 2(h) and the values are listed in Table 4. Figure 2 shows that the initial increase in $Fe^{2+}Oh$ found by XMCD is much larger than that suggested by the X-ray diffraction and Mössbauer methods used by Bosi et al. (2009) who report a maximum of ~1.1 atom Fe^{2+} in Oh at ~USP40, and by Hamdeh et al. (1999) who report a maximum of 1.1 atom Fe^{2+} in Oh at USP50. The results of Bosi et al. (2009) also suggest that significant Fe^{2+} enters tetrahedral sites at small USP contents with USP10 having 0.07 atoms Fe^{2+} in Td per 4 O rising to 0.267 by USP35. Hamdeh et al (1999) also report ~0.2 atoms Fe^{2+} in tetrahedral sites in USP30. In XMCD data reduction, peak area deconvolution for the octahedral Fe^{2+} component is very reliable, demonstrating that high contents of octahedral Fe^{2+} are indeed present in the titanomagnetite solid solution series. The data obtained from the XMCD spectra are also not consistent with earlier estimates for Fe^{2+} Td values which are about 5 times larger than the results for the USP30 sample. The XMCD site occupancy model in Figure 2h closely resembles the results of Akimoto (1957) in Figure 2c. However, Akimoto's model involved the incorporation of some Ti ions into the tetrahedral sites, whereas subsequent data has shown this to be unlikely (Fujino, 1974; Pearce et al., 2006; Wechsler et al., 1984). The results of the present

study indicate that variations of Fe^{3+} and Fe^{2+} between the tetrahedral and octahedral sites in titanomagnetites cannot be described using the simple models suggested by Akimoto (1954) and Néel-Chevallier (1955). Also, deviations from these models cannot simply be ascribed to difficulties involved in preparing homogeneous unoxidized titanomagnetites, as suggested by Wechsler et al. (1984) as the titanomagnetite samples synthesized in this study have been fully characterized in terms of their composition. From the data presented in this study, it can be seen that XMCD provides distinct spectral features for the entry Fe^{2+} and Fe^{3+} into both structural sites (Td and Oh) while with other techniques the information is derived from more convoluted arguments.

The XMCD site occupancy data for the 'stoichiometric' series have been used to calculate magnetic moments assuming magnetic moment values of 4.06 μ_B for Fe^{2+} and 5.0 μ_B for Fe^{3+} (Table 4) and plotted in Figure 12. From SQUID measurements the magnetic moment measured at 150K and 3T field for the USP75 sample was determined to be 0.79 μ_B, which is in good agreement with the value given in Table 4. The composition dependence of saturation moment for the present data differs from that of O'Reilly and Banerjee (1965), in which the saturation moment trend changes at ~20 and ~80% USP (Fig. 12), possibly relating to the introduction of Fe^{2+} into Td sites. For the present data, the samples fall on a linear trend from the magnetite end-member to USP45; this trend is steeper than that deduced by Hamdeh et al. (1999) but is not quite as steep as the Néel trend. The differences in the present data reflect that, over this composition range, a lower proportion of Fe^{2+} enters Oh than that suggested by Néel (1955) and a higher proportion than that deduced by Hamdeh et al. (1999). Above USP45, the data show a distinct change in trend and seem to approach the idealised model of Akimoto (1956) asymptotically. The O'Reilly and Banerjee (1965) and Lindsley (1976) data also approach the Akimoto trend at ~80%USP. In this study, the values for USP60 and USP90 are slightly higher than they should be, as these samples have slightly more oxidized compositions than the stoichiometric values (Table 4).

Site occupancy effects on cell parameter vs composition trends.

Earlier work has shown a sigmoidal trend in unit-cell edge *vs* ulvöspinel content with smaller rates of increase at the Ti-poor (USP0-20%) and Ti-rich (USP80-100) ends of the solid solution series than over the intermediate members (USP20-80) (e.g., Lindsley, 1965; Wechsler et al., 1984; Bosi et al., 2009). Fujino (1974), Weschsler et al. (1984) and Bosi et al. (2009) have also shown that refined T-O (Td) bond lengths increase steadily with increasing USP% while M-O(Oh) bondlengths show rather little change and Bosi et al. concluded that structural changes are mainly driven by changes in T-O rather than in M-O. Bosi et al. (2009) attribute the s-shaped trend in unit-cell edge to preferential entry of Fe^{3+} into Td at low USP contents and to preferential entry of Fe^{2+} into Oh at for high USP amounts. The XMCD occupancy data support the first relationship as only Fe^{3+} enters Td sites up to ~USP30 which would fix the T-O bondlength at ~1.89 Å thus limiting any increase in *a* over this composition range. However, the 'extra' amount of Fe^{2+} entering Oh increases the mean M-O bondlength (from 2.067 Å for USP0 to 2.077Å for USP30) even though entry of larger Fe^{2+} is coupled to that of smaller Ti. The cell parameter for this composition range is, therefore, controlled by the mean M-O bondlength rather than

that for T-O. Thus the overall effect of these site occupancies is to restrict the increase in a from USP0 to ~USP30, but once Fe^{2+} starts to enter Td the cell edge increases at a greater rate, as can be seen in Figure 3. The data in Fig. 3 do not show a decreased rate of change in unit-cell edge above USP75-80 and no evidence for this is observed in the XMCD site occupancy, largely because the USP90 sample is slightly too oxidized to provide entirely reliable site occupancies.

Site occupancy trends for titanomaghemite oxidation

As mentioned in the introduction, the maghemitization of titanomagnetites has a crucial effect on the magnetic properties of these phases and plays a clear role in determining the palaeomagnetic properties of crustal rocks. Many papers have been published on the mechanisms of these processes with particular attention being paid to whether the major process involves addition of oxygen, or removal of Fe (O'Reilly, 1984; O'Reilly and Banerjee, 1965; Xu et al., 1997). The different trends for these two processes are shown on Figure 1; the end-member formula for fully-oxidized ulvöspinel formed by addition of O is $Fe_{1.6}Ti_{0.8}\square_{0..6}O_4$, while that formed by removal of Fe is $Fe_{1.333}Ti_{1.0}\square_{0.666}O_4$. It has been suggested that hydrothermal alteration of ocean floor follows the Fe-loss mechanism, while synthesis experiments might be more likely to follow oxygen addition. The location of vacancies is important and ordering onto octahedral sites seems to be well established (e.g., Xu et al., 1997) but Collyer et al. (1988) assign a small vacancy content to Td.

XMCD has also been used to study site occupancies in magnetites variably oxidized to maghemite, and titanomagnetites oxidized towards titanomaghemites (Pearce et al., 2006). Pearce et al. (2006) also deduced that the XMCD results showed that vacancies in maghemitized magnetite and more chemically complex spinels occur only in octahedral sites in agreement with Gillot (1994). By contrast a slightly oxidized titanomagnetite appeared to have vacancies only in Td sites while more pervasively altered titanomaghemites contained vacancies in both Td and Oh sites. In order to address vacancy ordering in titanomagnetites, two as-synthesized samples (USP30, and 45) were buffered in the more oxidizing Ni-NiO buffer as well as in QFM. The latter samples are close to stoichiometric titanomagnetites but the former buffered samples should show some alteration to titanomaghemites. Data for the Ni-NiO samples are given in Table 4. For both samples, the QFM and Ni-NiO treatments show no significant change in the oxidation state in tetrahedral sites while for octahedral sites substantial increases in Fe^{3+} are balanced exactly by decreases in Fe^{2+}; Ti is assumed to remain constant. The differences between the QFM and Ni-NiO products for a given as-synthesised sample result from rapid equilibration of the same original sample surfaces with the appropriate buffer and must be related to addition of oxygen (from the buffer assemblage) rather than removal of Fe. The oxidation trends for these two samples are shown in Figure 7.
These experiments show clearly that, for the initial stages of oxygen addition, only octahedral Fe^{2+} is oxidised, and this in turn suggests that the resulting vacancies should also be restricted to the octahedral sites. Sample USP60 is slightly more oxidized than the stoichiometric value (Table 4) and this is reflected in anomalously small Fe^{2+}Oh and high Fe^{3+} Oh values (Figure 9) yet the occupancies for Td do not show significant displacements from the main trends. Such results also support the data suggesting that oxidation is predominantly restricted to the Oh sites.

Table 4 also gives vacancies calculated from XMCD Fe^{2+}/Fe^{3+} ratios determined for the different samples. All of the samples chosen as being close to stoichiometric have very small vacancy numbers, where the sample is more reduced than the stoichiometric oxidation state the vacancy number is –ve and where the sample is more oxidized than the stoichiometric value, the vacancy number is +ve. Much larger vacancy numbers are obtained for the maghemitized samples USP30NNO (0.088□/4 O) and USP45NNO (0.126□/ 4 O) compared to the 'stoichiometric' initial phases (~0). Zhou et al. (1999) have defined the degree of oxidation using the relationship $z = 3\square/(1+x)$ which shows that the surface of USP30NNO is about 20% oxidized while that for USP45NNO is 26% oxidized.

CONCLUDING REMARKS

XMCD provides detailed information on oxidation state and site symmetry of Fe ions in titanomagnetites and a new perspective on this interesting area of research. With a probing depth of ~4.5 nm (~6 unit cells), XMCD is ideally suited to the study of nanometer-scale materials and surfaces. As the substitution of Ti ions for Fe^{3+} ions in magnetite stabilizes the spinel structure and limits grain growth (Guigue-Millot et al., 2001) the Earth's crust contains nanometer-scale clusters of (often oxidized) titanomagnetites, particularly in soils associated with basaltic rocks (Soubrand-Colin et al., 2009). Thus, XMCD would be particularly relevant to the study of materials that define the paleomagnetic record, and there is potential to examine and understand the relationship between site occupancy and magnetic behaviour. In addition, it has been shown that, in the absence of surface passivation, these Fe^{2+}-bearing minerals are redox active and can reduce polyvalent metal contaminants (Lloyd et al., 2000) and thus XMCD can be used to provide information on how these materials interact with redox active species in the environment.

REFERENCES

Akimoto, S. (1954) Thermo-Magnetic Study of Ferromagnetic Minerals Contained in Igneous Rocks. Journal of Geomagnetism & Geoelectricity, 6(1), 1-14.
-. (1962) Magnetic Properites of $FeO-Fe_2O_3-TiO_2$ System as a Basis of Rock Magnetism. Journal of the Physical Society of Japan, 17, Supplement B-1, 706-710.

Akimoto, S., Katsura, T., and Yoshida, M. (1957) Magnetic Properites of $TiFe_2O_4$-Fe_3O_4 System and Their Change with Oxidation. Journal of Geomagnetism & Geoelectricity, 9(4), 165-178.

Arenholz, E., and Prestemon, S.O. (2005) Design and performance of an eightpole resistive magnet for soft Xray magnetic dichroism measurements. Review of Scientific Instruments, 78(6), 083908/18.

Banerjee, S.K. (1991) Magnetic properties of Fe-Ti oxides. In D.H. Lindsley, Ed. Oxide Minerals: Petrologic and Magnetic Significance, p. 107-128. Mineralogical Society of America, Washington D.C.

Binsted, N. (1998) Daresbury Laboratory EXCURV98 Program.

Binsted, N., Strange, R.W., and Hasnain, S.S. (1992) Constrained and restrained refinement in EXAFS data analysis with curved wave theory. Biochemistry, 31, 12117-12125.

Bleil, U., and Petersen, N. (1983) Variation in magnetization intensity and low-temperature titanomagnetite oxidation of ocean floor basalts. Nature, 301, 384-388.

Bosi, F., Hålenius, U., and Skogby, H. (2009) Crystal chemistry of the magnetite-ulvöspinel series. American Mineralogist, 94, 181-189.

Brice-Profeta, S., Arrio, M.-A., Tronc, E., Menguy, N., Letard, I., Cartier dit Moulin, C., Noguès, M., Chanéac, C., Jolivet, J.-P., and Sanctavit, P. (2005) Magnetic order γ-Fe_2O_3 nanoparticlesO: a XMCD study. Journal of Magnetism and Magnetic Materials, 288, 354-365.

Buddington, A.F., and Lindsley, D.H. (1964) Iron-titanium oxide minerals and synthetic equivalents. Journal of Petrology, 5(2), 310-357.

Chevallier, R., Bolfa, J., and Mathieu, S. (1955) Titanomagnetites et ilmenites ferromagnetiques. Bulletin du societe francais Mineralogie et Cristallographie,, 78, 307-346.

Coker, V.S., Pearce, C.I., Pattick, R.A.D., van der Laan, G., Telling, N.D., Charnock, J.M., Arenholz, E., and Lloyd, J.R. (2008) Probing the site occupancies of Co-, Ni-, and Mn-substituted biogenic magnetite using XAS and XMCD. American Mineralogist, 93, 1119-1132.

Coker, V.S., Telling, N.D., van der Laan, G., Pattick, R.A.D., Pearce, C.I., Arenholz, E., Tuna, F., Winpenny, R., and Lloyd, J.R. (2009) Harnessing the Extracellular Bacterial Production of Nanoscale Cobalt Ferrite with Exploitable Magnetic Properties. ACS Nano, in press.

Cornell, R.M., and Schwertmann, U. (2003) The iron oxides. Structure, properties, reactions, occurrences and uses. Wiley-VCH, Weinheim.

Fujino, K. (1974) Cation distribution and local variation of sity symmetry in solid solution series, Fe_3O_4-Fe_2TiO_4. Mineralogical Journal, 7(5), 472-488.

Gillot, B. (1994) Infrared spectrometric investigation of submicron metastable cation-deficient spinels in relation to order-disorder phenomena and phase transition. Vibrational Spectroscopy, 6, 127-148.

Goodenough, J.B., and Loeb, A.L. (1955) Theory of ionic ordering, crystal distortion, and magnetic exchange due to covalent forces in spinels. Physical Review, 98, 391-408.

Guigue-Millot, N., Champion, Y., Hytch, M.J., Bernard, F., Bégin-Colin, S., and P. Perriat, P. (2001) Chemical Heterogeneities in Nanometric Titanomagnetites Prepared by Soft Chemistry and Studied Ex Situ: Evidence for Fe-Segregation and Oxidation Kinetics. Journal of Physical Chemistry B, 105, 7125-7132.

Gurman, S.J., Binsted, N., and Ross, I. (1984) A rapid, exact, curved-wave theory for EXAFS calculations. Journal of Physics C, 17, 143-151.

Hamdeh, H.H., Barghout, K., Ho, J.C., Shand, P.M., and Miller, L.L. (1999) A Mössbauer evaluation of cation distribution in titanomagnetites. Journal of Magnetism and Magnetic Materials, 191, 72-78.

Hedin, L., and Lundqvist, S. (1969) Effects of electron-electron and electron-phonon interactions on the one-electron states of solids. Solid State Physics, 23, 1-181.

Henderson, C.M.B., Charnock, J.M., and Plant, D.A. (2007) Cation occupancies in Mg, Co, Ni, Zn, Al ferrite spinels: a multi-element EXAFS study. Journal of Physics: Condensed Matter, 19, 1-25.

Kakol, Z., Sabol, J., and Honig, J.M. (1991) Cation distribution and magnetitc properties of titanomagnetites $Fe_{3-x}Ti_xO_4$ (0<x<1). Physical Review B, 43, 1.

Lindsley, D. (1976) The crystal chemistry and structure of oxide minerals as exemplified by the Fe-Ti oxides. Reviews in Mineralogy, Mineralogical Society of America, 3, Ll-60.

Lloyd, J.R., Sole, V.A., Van Praagh, C.V.G., and Lovley, D.R. (2000) Direct and Fe(II)-mediated
reduction of technetium by Fe(III)- reducing bacteria. Applied and Environmental Microbiology, 66, 3743-3749.

Néel, L. (1955) Some theoretical aspects of rock-magnetism. Advances in Physics, 54(191-243).

O'Reilly, W. (1984) Rock and Mineral Magnetism. Blackie & Son Limited, Glasgow.

O'Reilly, W., and Banerjee, S.K. (1965) Cation distribution in titanomagnetites (1-x)Fe_3O_4 - $x$$Fe_2TiO_4$. Physics Letters, 17, 237-238.

Pattrick, R.A.D., van der Laan, G., Henderson, C.M.B., Kuiper, P., Dudzik, E., and Vaughan, D.J. (2002) Cation site occupancy in spinel ferrites studied by Xray magnetic circular dichroism: developing a method for mineralogists. European Journal of Mineralogy, 14, 1095-1102.

Pearce, C.I., Henderson, C.M.B., Pattick, R.A.D., van der Laan, G., and Vaughan, D.J. (2006) Direct determination of cation site occupancies in natural ferrite spinels by $L_{2,3}$ x-ray absorption spectroscopy and x-ray magnetic circular dichroism. American Mineralogist, 92, 880-893.

Pellegrin, E., Hagelstein, M., Doyle, S., Moser, H.O., Fuchs, J., Vollath, D., Schuppler, S., James, M.A., Saxena, S.S., Nielsen, L., Rogojanu, O., Sawatzky, G.A., Ferrero, C., Borowski, M., Tjernberg, O., and Brookes, N. (1999) Characterization of nanocrystalline ã-Fe_3O_4 with synchrotron radiation techniques. Physica Status Solidi B, 215, 797-801.

Schedin, F., Morrall, P., Petrov, V.N., Case, S., Thomas, M.F., Dudzik, E., van der Laan, G., and Thornton, G. (2000) Magnetic properties of ultrathin epitaxial Fe_3O_4 films on Pt(111). Journal of Magnetism and Magnetic Materials, 211, 266-270.

Signorini, L., Pasquini, L., Boscherini, F., Bonetti, E., Letard, I., Brice-Profeta, S., and Sanctavit, P. (2006) Local magnetism in granular iron/iron oxide nanostructures by phase- and site-selective x-ray magnetic circular dichroism. Physical Review B, 74, 014426.

Soubrand-Colin, M., Horen, H., and Courtin-Nomade, A. (2009) Mineralogical and magnetic characterisation of iron titanium oxides in soils developed on two various basaltic rocks under termperate climate. Geoderma, 149, 27-32.

van der Laan, G. (1990) Polaronic satellites in X-ray absorption spectra. Physical Review B, 41, 12366 - 12368.

van der Laan, G., and Kirkman, I.W. (1992) The 2p absorption spectra of 3d transition metal compounds in tetrahedral and octahedral symmetry. Journal of Physics: Condensed Matter, 4, 4189-4204.

van der Laan, G., and Thole, B.T. (1991) Strong magnetic Xray dichroism in 2p absorption spectra of 3d transition metal ions. Physical Review B, 43, 13401-13411.

Verwey, E.J.W., and Heilman, E.L. (1947) Physical Properties and Cation Arrangements of Oxides with Spinel Structures: I. Cation Arrangement in Spinels. The Journal of Chemical Physics, 15(4), 174-180.

Wechsler, B.A., Lindsley, D.H., and Prewitt, C.T. (1984) Crystal stucture and cation distribution in titanomagnetites ($Fe_{3-x}Ti_xO_4$). American Mineralogist, 69, 754-770.

Wilson, A.D. (1955) A new method for the determination of ferrous iron in rocks and minerals. Bulletin Geological Survey Great Britain, 9, 56-58.

Xu, W., Peacor, D.R., Dollase, W.A., van de Voo, R., and Beaubouef, R. (1997) Transformation of titanomagnetite to titanomaghemite: A slow, two-step, oxidation-ordering process in MORB. American Mineralogist, 82, 1101-1110.

Zhou, W., Van der Voo, R., and Peacor, D.R. (1999) Preservation of pristine titanomagnetite in older ocean-floor basalts and its significance for paleointensity studies. Geology, 27, 1043–1046.

Zhou, W., Van der Voo, R., Peacor, D.R., Wang, D., and Zhang, Y. (2001) Low-temperature oxidation of titanomagnetite to titanomaghemite in MORB: a gradual process with implications for marine magnetic anomaly amplitudes. Journal of Geophysical Research, 106, 6409–6421.

LIST OF TABLES

Table 1. Review of published models for cation site ordering in titanomagnetites

Table 2. Microprobe and chemical analyses and unit cell parameters for titanomagnetite solid-solutions

Table 3. Pre-edge, edge and refined EXAFS data for magnetite and three titanomagnetite samples

Table 4. Site occupancies from XMCD, calculated vacancies and magnetic moments (μ_B)

FIGURES

Figure 1. Phases in the system Fe^{2+}-Fe^{3+}-Ti^{4+}, showing the major solid-solution series magnetite-ulvöspinel, hematite-ilmenite and ferropsuedobrookite-psuedobrookite (after Buddington and Lindsley, 1964)

Figure 2: Site occupancy models for Fe^{2+} (■)and Fe^{3+} (▲) in tetrahedral and Fe^{2+} (●)and Fe^{3+} (X) in octahedral (Oh) sites: (A) Akimoto (1954), (B) Néel (1955), (C) Akimoto (1957), (D) O'Reilly (1965), (E) Kakol (1991), (F) Hamdeh (1999), (G) Bosi (2009) and (H) the present study

Figure 3: Variation of unit cells parameters with composition

Figure 4: XANES Figure. (Black or solid line) end-member magnetite MT6P, (green or — – — –) 30% USP, (blue or — — —) 60% USP, (red or – – – –) 90% USP

Figure 5: EXAFS (top) + Ft (bottom) Figure. Solid lines experimental data, broken lines fits: (i) end-member magnetite MT6P, (ii) 30% USP, (iii) 60% USP, (iv) 90% USP

Figure 6: Temperature dependence of the magnetization of the synthetic titanmagnetite series in a field $H = 100$ Oe, relative to the magnetization at 5K

Figure 7: Experiemental Ti $L_{2,3}$-edge XAS spectra for synthetic magnetite – ulvöspinel solid solutions series.

Figure 8: Experimental Fe $L_{2,3}$-edge XMCD spectra (black lines) and best-fit calculated spectra, based on the four theoretical site components, (red lines) for USP0, USP15, USP30, USP45, USP60, USP75 and USP90.

Figure 9: Ternary oxidation plot relative to stoichiometric trend

Figure 10: (A) Experimental Fe L_3-edge XMCD spectra (black circles) with best-fit spectra (red line) for (i) USP30 and (ii) USP75. (B) For the best-fit spectrum of each sample, the decomposition into the spectra for the Fe^{2+} T_d, Fe^{2+} O_h, Fe^{3+} T_d, and Fe^{3+} O_h components is given.

Figure 11: Site occupancy models for Fe^{2+} (■)and Fe^{3+} (▲) in tetrahedral and Fe^{2+} (●)and Fe^{3+} (**X**) in octahedral (Oh) sites, from XMCD data.

Figure 12: Composition dependence of saturation moment. The broken lines present the models of Akimoto, O'Reilly-Banerjee and Néel-Chevallier.

Ti

FeTi$_2$O$_5$

FeTiO$_3$

Fe$_2$TiO$_4$

Fe$_{1.33}$Ti$_{1.0}$□$_{0.67}$O$_4$

Fe loss

Fe$_{1.6}$Ti$_{0.8}$□$_{0.6}$ (Fe$_2$TiO$_5$)

O addition

USP60

Fe loss

Fe$_{1.87}$Ti$_{0.6}$□$_{0.53}$O$_4$

O addition Fe$_{2.0}$Ti$_{0.5}$□$_{0.50}$O$_4$

Titanomagnetites

Titanomaghemites

Fe^{2+}

FeO
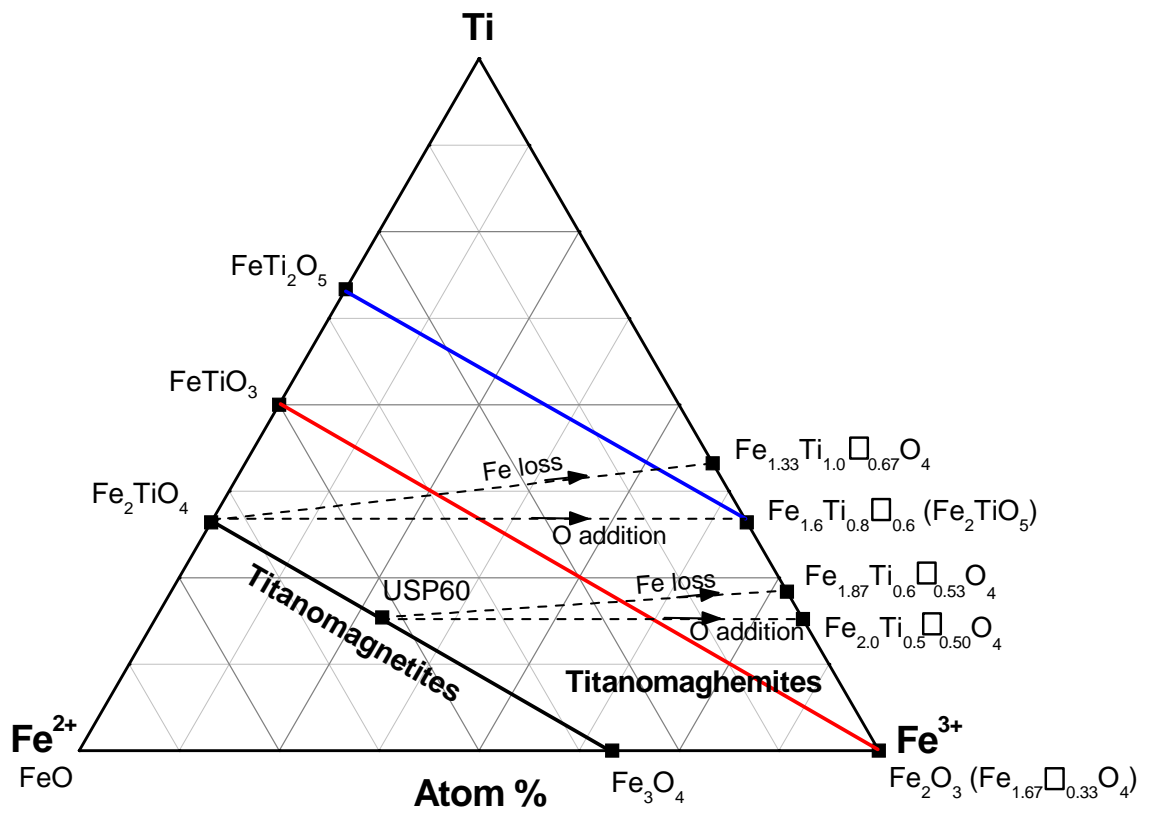
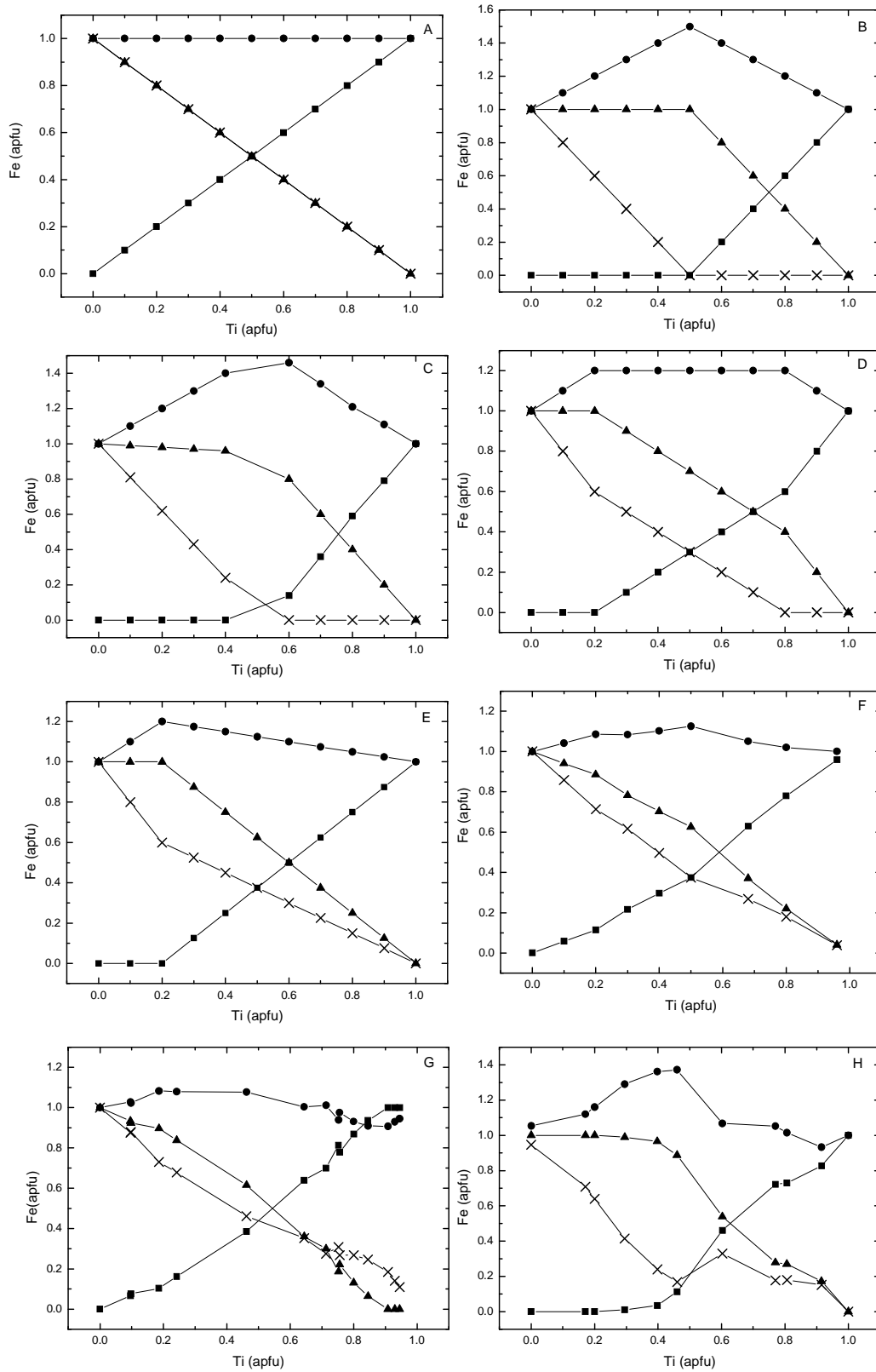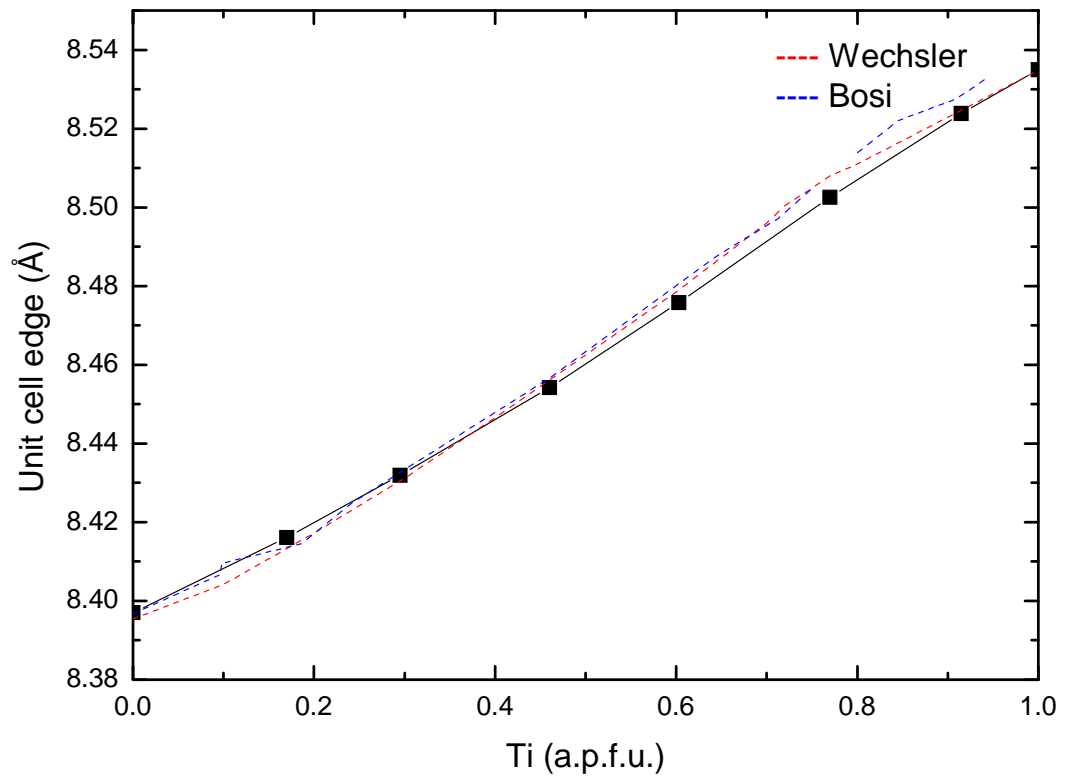**Atom %**

Fe$_3$O$_4$

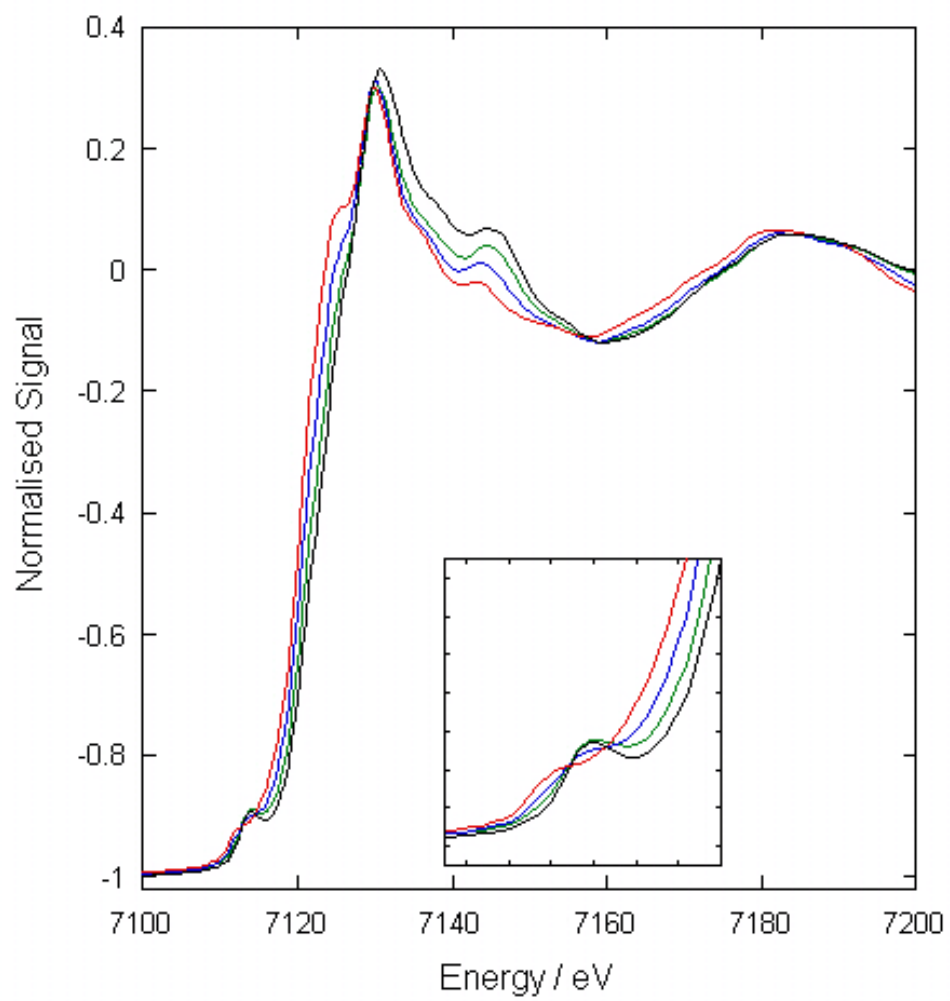**Fe^{3+}**
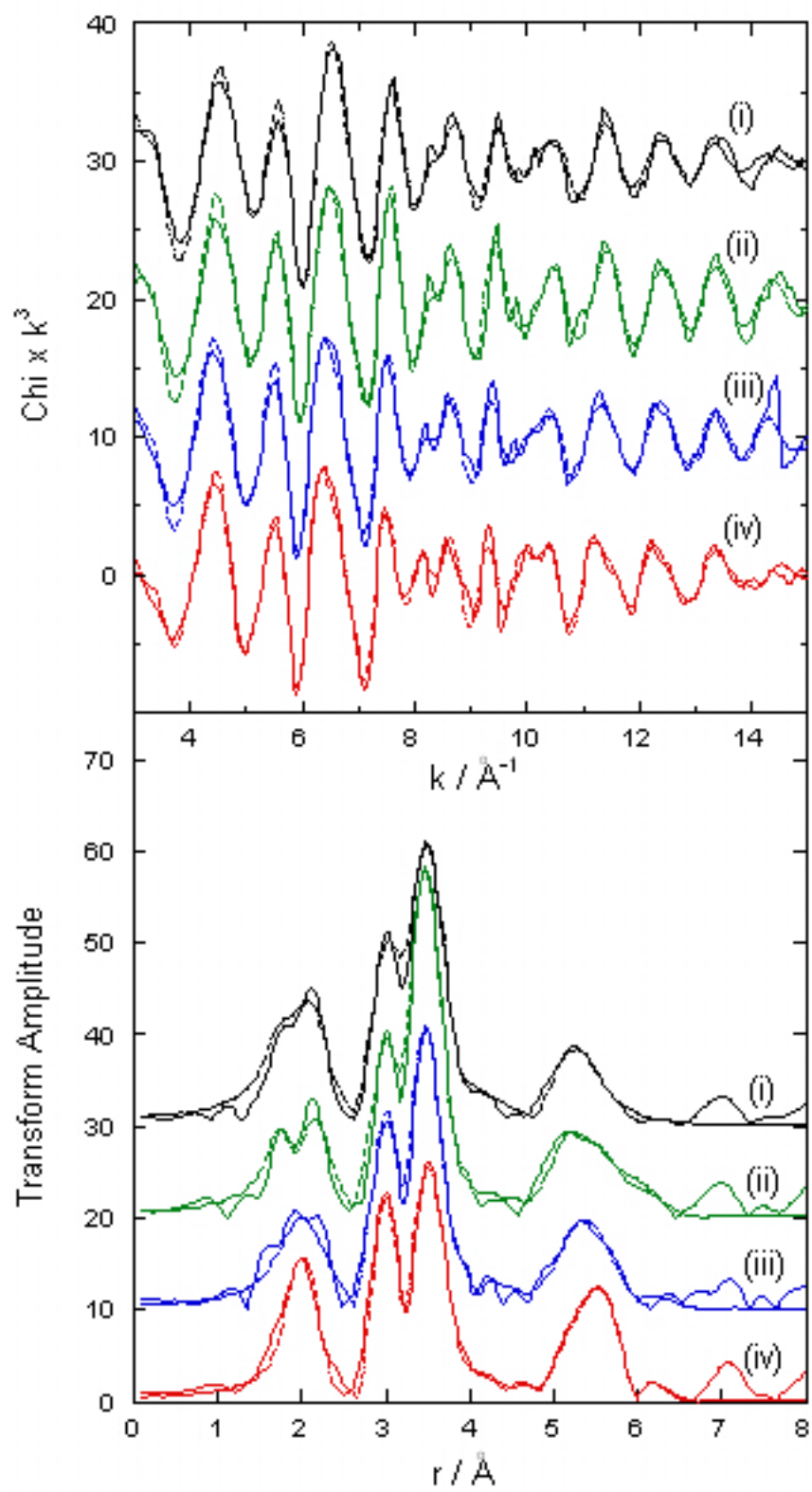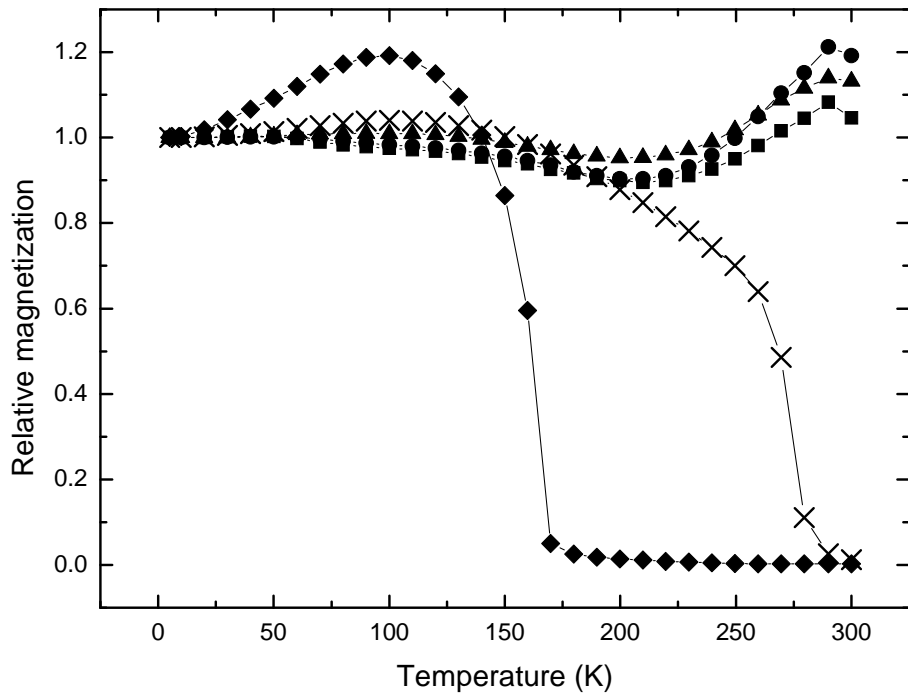
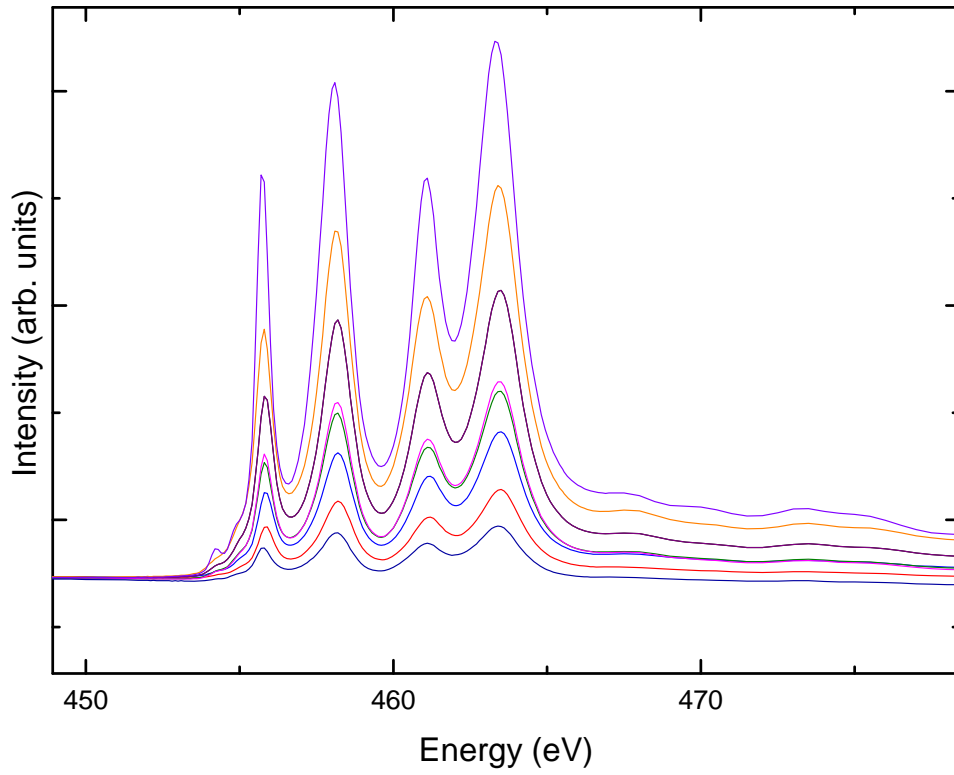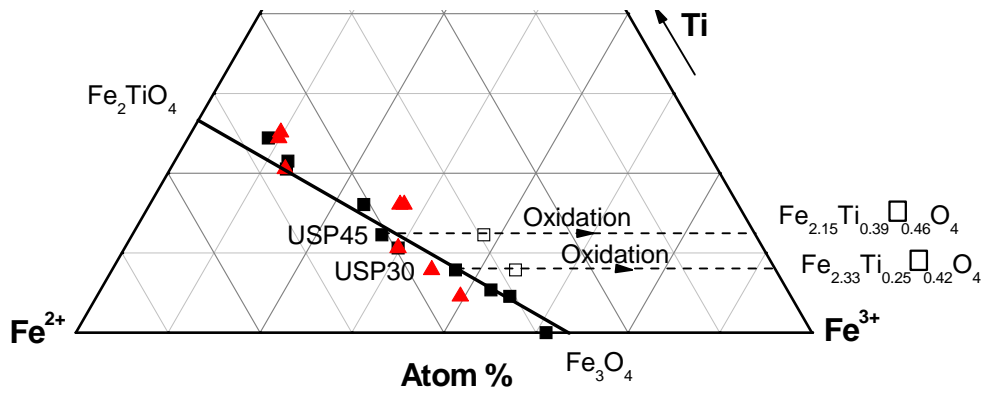Fe$_2$O$_3$ (Fe$_{1.67}$□$_{0.33}$O$_4$)

Figure 1

Figure 2

Figure 3

Figure 4

Figure 5

Figure 6

Figure 7

Figure 8

USP0

USP15

USP30

USP45

USP60

USP75

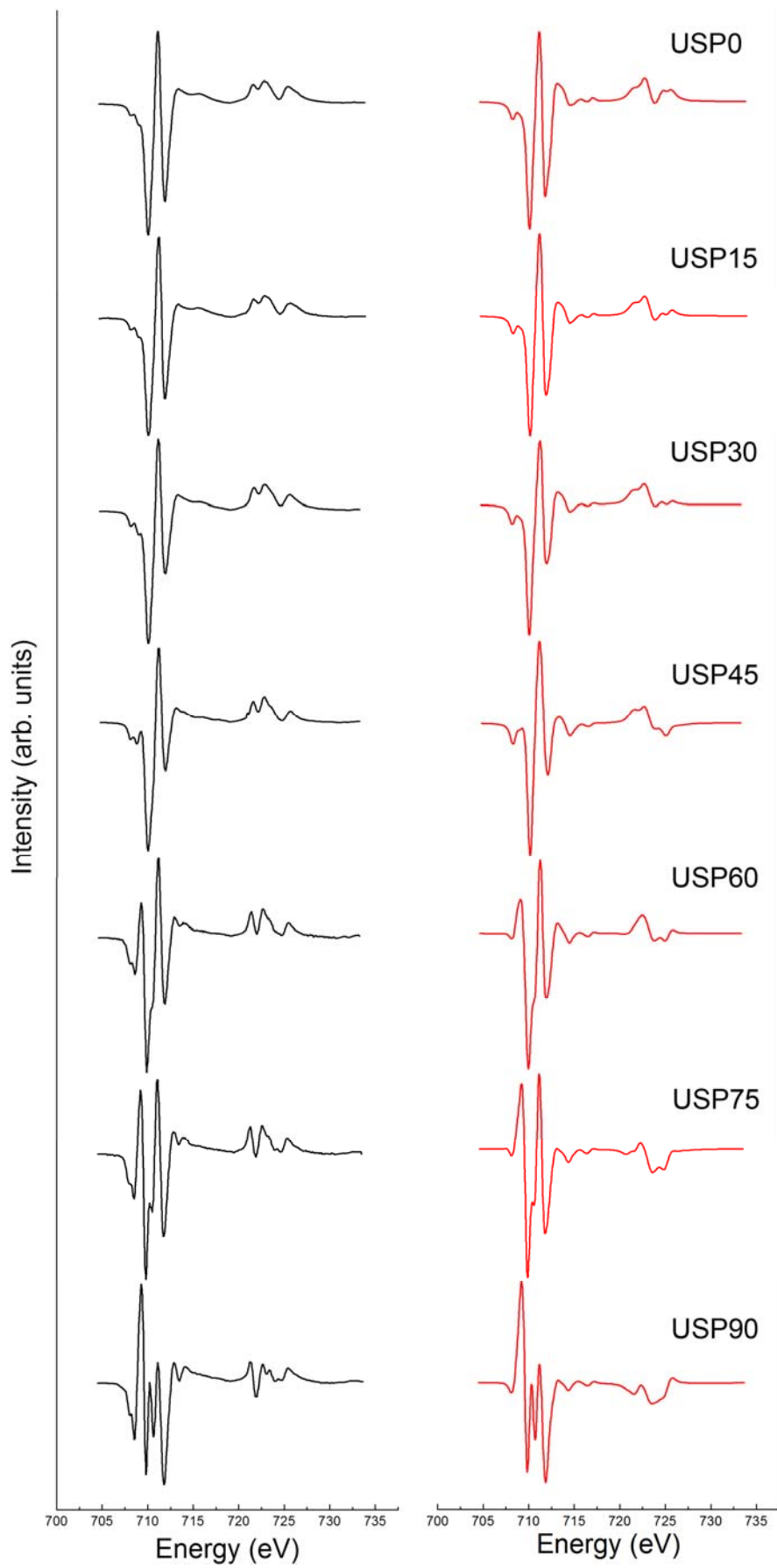USP90

Intensity (arb. units)

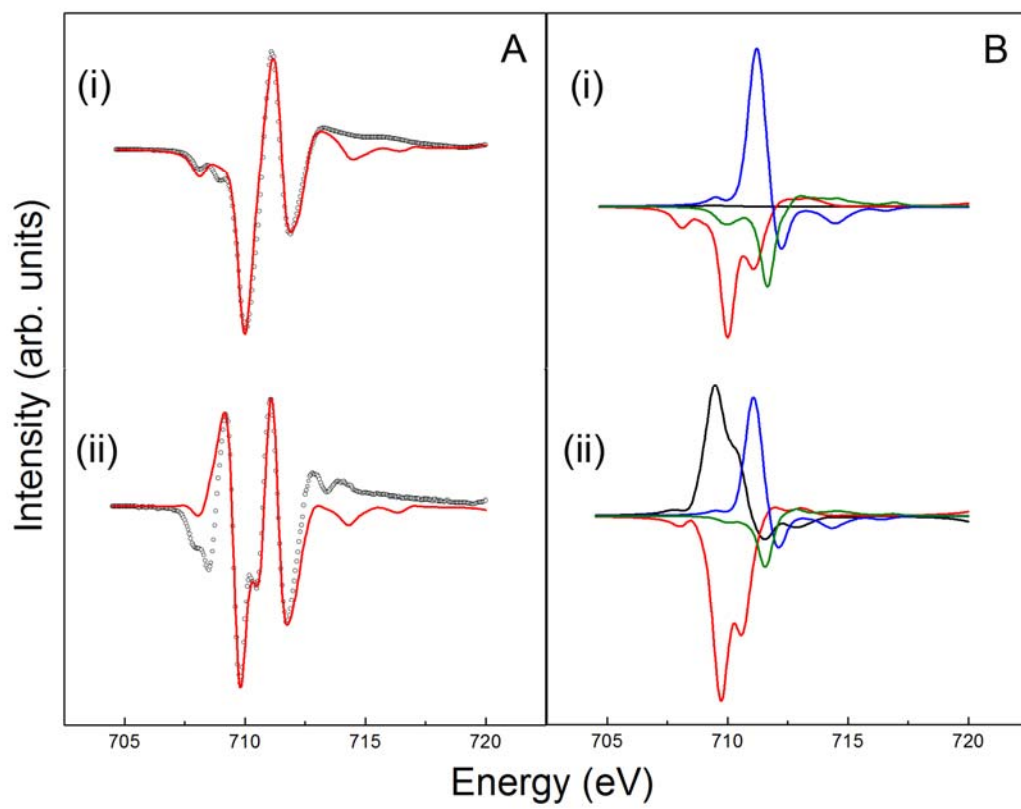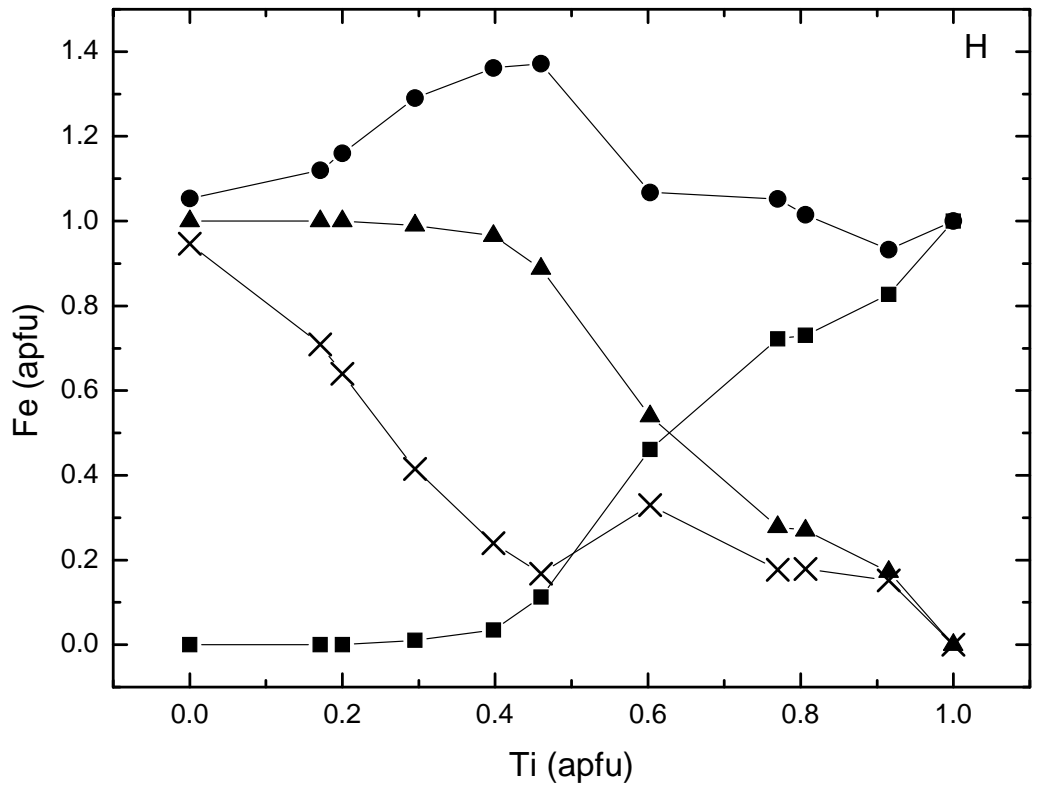Energy (eV)

Energy (eV)

Figure 9

Figure 10

Figure 11
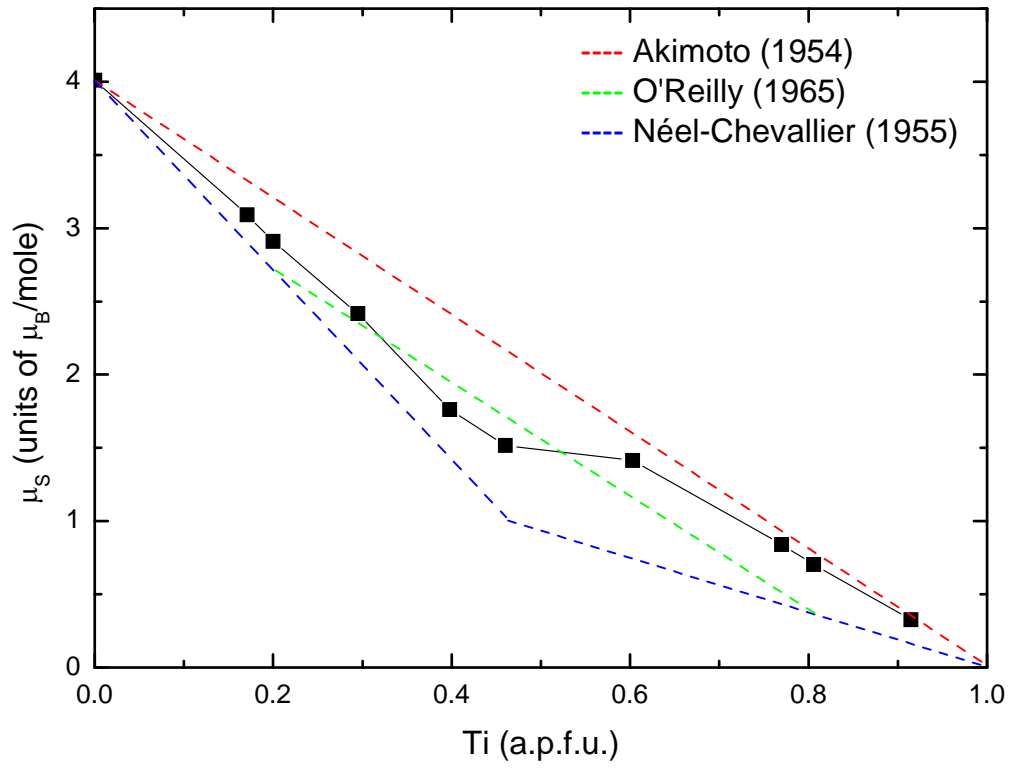
Figure 12

Table 1. Review of published models for cation site ordering in titanomagnetites

Model	Samples	Technique	Summary	Reference
A	Ferromagnetic minerals separated from igneous rocks	Chemical composition, unit-cell parameter, saturation magnetization, Curie point (magnetic balance, 3kOe)	Concentration of Fe^{2+} and Fe^{3+} ions on both sites varies linearly with x $Fe^{3+}_{1-x}Fe^{2+}_{x}(Fe^{2+}Fe^{3+}_{1-x}Ti^{4+}_{x})O^{2-}_{4}$	(Akimoto, 1954)
B	Theoretical study	Verwey's empirical law	Ti^{4+} ions always occupy octahedral sites. Remaining octahedral sites filled by Fe^{2+} ions.	(Chevallier et al., 1955; Néel, 1955)
C	Fe_2O_3, TiO_2 and Fe powders heated under vacuum in silica tubes; 6 hrs at 1150˚C	Chemical composition, unit-cell parameter, saturation magnetization, Curie point (magnetic balance, 3kOe)	Cation distribution given by $Fe^{3+}_{1-a}Ti^{4+}_{a}(Fe^{2+}_{1+x}Fe^{3+}_{1-2x+a}Ti^{4+}_{x-a})O^{2-}_{4}$ for $x = < 0.5$ and $Fe^{3+}_{2-2x}Fe^{2+}_{2x-1-a}Ti^{4+}_{a}(Fe^{2+}_{2-x+a}Ti^{4+}_{x-a})O^{2-}_{4}$ for $x = > 0.5$	(Akimoto et al., 1957)
D	Sintered mixtures of Fe_2O_3, TiO_2 and Fe	Saturation magnetization (vibrating sample magnetometer, 30kOe), electrical conductivity (four probe method)	For $0 < x < 0.2$, Fe^{3+} preferentially in tetrahedral sites. Cation distribution given by $Fe^{2+}_{x-0.2}Fe^{3+}_{1.2-x}(Fe^{2+}_{1.2}Fe^{3+}_{0.8-x}Ti^{4+}_{x})O^{2-}_{4}$ for $0.2 < x < 0.8$. All Fe^{3+} located in tetrahedral sites for $0.8 < x < 1$	(O'Reilly and Banerjee, 1965)
E	Mixtures of Fe_2O_3, TiO_2 and Fe sponge sintered in Ag-foil lined evacuated SiO_2-glass tubes at 930˚C for 4-7 days	Chemical composition, unit-cell parameter, oxygen coordinate, thermal parameters, sublattice magnetizations (neutron diffraction), hysteresis loops, saturation magnetization (vibrating sample magnetometer, 20kOe)	Fe^{2+}-Fe^{3+} site occupancies vary linearly with composition, consistent with Akimoto (1954)	(Wechsler et al., 1984)
F	Single crystals grown in CO-CO_2 atmosphere	Chemical composition, magnetization curves, hysteresis loops (vibrating sample magnetometer, 15kOe)	Cation distribution given by $Fe^{3+}(Fe^{3+}_{1-2x}Fe^{2+}_{1+x}Ti^{4+}_{x})O^{2-}_{4}$	(Kakol et al., 1991)

			for $0 \leq x \leq 0.2$ and $Fe^{3+}_{1.25-1.25x}Fe^{2+}_{1.25x-0.25}(Fe^{3+}_{0.75-0.75x}Fe^{2+}_{1.25-0.25x}Ti^{4+}_{x})O^{2-}_{4}$ for $0.2 < x \leq 1$	
G	Stoichiometric mixtures of Fe_2O_3 and TiO_2 heated at $1000^{o}C$ (note no information given of redox control)	Mössbauer spectroscopy at 4.2K in 70 kOe applied field	Cation distribution given by $Fe^{3+}_{f(3-x)}Fe^{2+}_{1-f(3-x)}(Fe^{3+}_{2(1-x)-f(3-x)}Fe^{2+}_{x+f(3-x)}Ti_x)O_4$ with $f = 0.333(1-0.25x)$ for $0<x<0.2$; $f = 0.35(1-0.57x)$ for $(0.3<x<0.5)$; and $f = 0.50(1-x)$ for $(0.5<x<1)$	(Hamdeh et al., 1999)
H	Single crystals grown in CO_2 and H_2; slow cooling from 1200-900˚C	Unit-cell parameter, chemical composition, $Fe^{3+}/\sum Fe$-ratios (Mössbauer spectroscopy)	Cation distribution split into two contributions: a linear trend due to $Fe^{3+}\ T_d + Fe^{3+}\ O_h = Fe^{2+}\ T_d + Ti^{4+}\ O_h$ chemical substitution and a non-linear trend due to internal electron exchange	(Bosi et al., 2009)

Table 2. Microprobe and chemical analyses and unit cell parameters for titanomagnetite solid solutions

	USP0/2	USP15/2	USP20/1	USP30/2	USP40/1	USP45/2	US60/1	USP60/2	USP75/2	USP80/1	USP90/2	USP100/2
Mean of n analyses	10	12	12	9	15	8	8	10	10	10	8	10
TiO_2	0.04(.02)	5.8(.1)	6.91 (.07)	10.3 (.1)	13.9 (.2)	15.7 (.2)	20.8 (.1)	20.1 (.7)	26.5 (.5)	28.5 (.4)	32.0 (.3)	33.5 (.2)
FeO	91.1 (.5)	86.4(1.0)	87.1 (.6)	84.8 (.2)	81.4 (.7)	78.0 (.6)	74.2 (.5)	71.9 (2.0)	68.9 (1.0)	69.6 (.6)	65.5 (.5)	65.8 (.5)
Total	91.1	92.2	94.0	95.1	95.3	93.7	95.0	92.0	95.4	98.1	97.5	99.3
Cats (32O & 24 cats)												
Fe^{3+}	15.981	13.267	12.803	11.273	9.622	8.647	6.337	6.350	3.679	3.098	1.363	0.925
Fe^{2+}	8.009	9.366	9.598	10.363	11.189	11.677	12.832	12.825	14.160	14.451	15.318	15.537
Ti	0.009	1.366	1.598	2.363	3.189	3.677	4.832	4.825	6.160	6.451	7.318	7.537
USP%	0.1	17.1	20.0	29.5	39.8	46.0	60.3	60.3	77.0	80.6	91.5	94.2
FeO wt% calc	31.1	35.0	37.5	40.6	44.0	46.0	50.8	50.8	56.4	57.7	61.4	62.3
FeO wt% chem.anal	29.8	37.0	n.a.	40.4	n.a.	44.9	n.a.	47.0	54.2	n.a.	59.1	57.1
Unit cell edge, Å	8.3987 (6)	8.4161 (6)	8.4153 (7)	8.4319 (6)	8.4410 (8)	8.4542 (3)	8.4746 (9)	8.4758 (6)	8.5026 (7)	8.5056 (7)	8.5238 (5)	8.5296 (4)
USP % from c Akimoto (1957)	5.8	18.1	17.5	29.5	35.3	45.2	58.6	60.1	78.4	80.1	92.6	96.5

Table 3. Pre-edge, edge and refined EXAFS data for magnetite and three titanomagnetite samples

Sample	Pre-edge Height ±0.005	Pre-edge eV	Energy at ½ edge height eV	Shell 1 Fe-O_{tet} ±0.01		Shell 2 Fe-O_{oct} ±0.01		Shell 3 Fe_{oct}-Fe/Ti_{oct}		Shell 4 Fe_{tet}-Fe/Ti_{oct} + Fe_{oct}-Fe_{tet}	
				r	$2\sigma^2$	r	$2\sigma^2$	r	$2\sigma^2$	r	$2\sigma^2$
Magnetite[*]	0.050	7113.9	7123.5	1.89	0.012	2.05	0.022	2.99	0.023	3.50	0.020
30% USP	0.045	7113.9	7123.2	1.89	0.016	2.08	0.022	3.01	0.019	3.51	0.012
60% USP	0.030	7113.5	7122.5	1.92	0.026	2.08	0.025	3.00	0.016	3.51	0.014
90% USP	0.025	7112.2	7121.8	1.99	0.030	2.09	0.036	3.00	0.013	3.53	0.015

Pre-edge and edge positions w.r.t. Fe foil 1st peak in derivative defined as 7111.1 eV.
[*] Mean of values for MT873, MT855, and MT6P

Table 4. Site occupancies from XMCD, calculated vacancies and magnetic moments (μ_B)

Sample name	Ulvo-spinel %	Experimental site occupancies					Expt. 2+/ΣFe	Stoichio. 2+/ΣFe	Site occupancies (Td = 1; Oh = 2)					Vacancies / 4O	Calculated magnetic moment
'Stoichiometric' series		Fe^{2+} Td	Fe^{2+}Oh	Fe^{3+} Td	Fe^{3+}Oh	Ti Oh			Fe^{2+} Td	Fe^{2+}Oh	Fe^{3+} Td	Fe^{3+}Oh	Ti Oh		
USP0/2 QFM	0	0	1.08	0.94	0.97	0	0.360	0.333	0	1.05	1.00	0.95	0	- 0.027	4.01
USP15/2 NNO	17.1	0	1.15	0.96	0.72	0.17	0.405	0.414	0	1.12	1.00	0.71	0.17	+0.009	3.09
USP20/1 SYN	20.0	0	1.21	0.93	0.67	0.20	0.431	0.429	0	1.16	1.00	0.64	0.20	- 0.002	2.91
USP30/2 QFM	29.5	0.011	1.29	0.84	0.56	0.30	0.482	0.479	0.012	1.19	0.99	0.51	0.30	- 0.002	2.42
USP40/1 SYN	39.8	0.031	1.46	0.86	0.26	0.40	0.572	0.537	0.034	1.36	0.97	0.24	0.40	- 0.034	1.76
USP45/2 QFM	46.0	0.11	1.42	0.84	0.17	0.46	0.599	0.575	0.11	1.37	0.89	0.17	0.46	- 0.026	1.52
USP60/2 QFM	60.3	0.47	1.07	0.55	0.33	0.60	0.636	0.669	0.46	1.07	0.54	0.33	0.60	+0.025	1.41
USP75/2 WM(F)	77.0	0.82	0.94	0.32	0.16	0.77	0.788	0.794	0.72	1.05	0.28	0.18	0.77	+0.006	0.84
USP80/1 SYN	80.6	0.81	0.93	0.30	0.16	0.81	0.790	0.823	0.73	1.02	0.27	0.18	0.81	+0.026	0.71
USP90/2 WM(F)	91.5	0.90	0.85	0.19	0.14	0.92	0.843	0.918	0.83	0.93	0.17	0.15	0.92	+0.062	0.33
'Oxidised' samples															
USP30/2 NNO	29.5	0.012	1.05	0.94	0.71	0.30	0.391	0.479	0.013	1.02	0.99	0.69	0.30	+0.086	2.58
USP45/2 NNO	46.0	0.12	0.98	0.92	0.52	0.46	0.436	0.575	0.11	1.01	0.88	0.53	0.46	+0.129	1.86